The vertical structure of the wave bottom boundary layer over a sloping bed

The Vertical Structure of the Wave Bottom Boundary Layer over a Sloping Bed: Theory and Field Measurements

QINGPING ZOU AND ALEX E. HAY

Department of Oceanography, Dalhousie University, Halifax, Nova Scotia, Canada

(Manuscript received 31 July 2001, in final form 20 December 2002)

ABSTRACT

Theoretical solutions for the wave bottom boundary layer (WBL) over a sloping bed are compared with field measurements in the nearshore zone. The WBL theory is constructed using both viscoelastic–diffusion and conventional eddy viscosity turbulent closure models. The velocity solutions are then matched with those of the interior flow, given by Chu and Mei potential theory for surface gravity waves over a sloping bottom. The field measurements were obtained with a coherent Doppler profiler over a 2° bed slope. Results are presented for both flat and rippled bed conditions, the latter being characterized by low steepness, linear transition ripples. Close to the bed, the observed velocity profiles change rapidly in amplitude and phase relative to potential flow theory, indicating the presence of a wave boundary layer with a thickness of 3–6 cm. The observed velocity and shear stress profiles are in good agreement with the theory. The sloping bottom has significant effects on the vertical velocity, but not on the horizontal velocity and shear stress. Bottom roughness and friction velocity are estimated from optimizing the model–data comparisons. The friction velocities and wave friction factors are found to be consistent with values obtained from the momentum integral method and from the nearbed turbulence intensity, and with Tolman's semiempirical formulation.

1. Introduction

As surface gravity waves propagate toward shore into the shoaling region, they are characterized by larger amplitudes and narrower directional distributions. An intensified oscillatory turbulent bottom boundary layer is generated, which plays a key role in transporting sediment and the consequent evolution of nearshore morphology (Nielsen 1992; Fredsoe and Deigaard 1992). The wave turbulent boundary layer also has a significant effect on wave dissipation in coastal environments (Tolman 1994; Young and Gorman 1995; Ardhuin et al. 2001).

In turbulent oscillatory flow, the boundary layer thickness is limited by the time available for newly generated turbulence to diffuse away from the bed during each half cycle. Using the wave half-period as the timescale available for growth and the bottom friction velocity u_* as the boundary layer growth rate, the wave bottom boundary layer (WBL) thickness δ is roughly $u_*/2f$, where f is the wave frequency. In the coastal zone, u_* is typically a few centimeters per second and wave periods are around 10 s. Accordingly, the WBL is expected to be only 5–10 cm thick. Resolving the vertical structure of such a thin layer under field conditions is quite challenging, especially over mobile beds for which the local bed elevation and bedforms may both evolve with time. It is only quite recently that suitable measurement techniques have become available.

Quantitative predictions of the processes occurring within the WBL depend on the choice of Reynolds stress closure model. In the past decade, many different models have been proposed to describe the vertical structure of the WBL (see Sleath 1990; Nielsen 1992; Fredsoe and Deigaard 1992 for reviews). Among these models, only eddy viscosity models have yielded analytical solutions. Kajiura used a time-invariant eddy viscosity proportional to the distance from the bed and later a more elaborate, triple layer formulation (Kajiura 1968), obtaining an ensemble average velocity that was in reasonable agreement with the existing measurements at the time. Solutions based on other time-invariant eddy viscosity forms were later postulated by Johns (1969), Grant (1977), Smith (1977), Brevik (1981), and Myrhaug (1982). To incorporate the unsteadiness of the oscillatory flow, time-varying eddy viscosities have been suggested by Lavelle and Mofjeld (1983), Trowbridge and Madsen (1984), Davies (1986), and Madsen and Wikramanayake (1991), and have been shown to improve the model–data comparisons of the second harmonics and streaming velocity but not on the first harmonics.

Conventional eddy viscosity and mixing length models are based on the assumption that the turbulence is

Corresponding author address: Dr. Qingping Zou, Department of Oceanography, Dalhousie University, Halifax, NS B3H 4J1, Canada. E-mail: qingping.zou@dal.ca

in local equilibrium with ambient mean flow, with production equal to dissipation. As shown by the laboratory studies of oscillatory turbulent boundary layers over rough and smooth beds, as flow starts to accelerate, turbulence is generated at the bed and propagates upwards; as flow starts to decelerate, turbulence is intensified by the adverse pressure gradient, moves upward and dissipates until the flow reversal (Sleath 1987; Jensen et al. 1989). These results suggest that the time and space distributions of production and dissipation differ in this type of boundary layer. It follows that turbulent relaxation and diffusion effects are likely to be important, and more sophisticated models are necessary to adequately describe the vertical profiles of the ensemble-mean motion and turbulence properties.

Bradshaw et al. (1967) and Townsend (1972) converted the turbulent energy equation into a turbulent shear stress equation by relating turbulent intensity, relaxation, diffusion, and dissipation to the shear stress. Based on Townsend's turbulent shear stress equation, Zou (1995, 1998) derived a viscoelastic model (the eddy viscosity model with a turbulent relaxation term added, leading to a complex effective eddy viscosity) for steady turbulent boundary layers over undulating topography. Zou (2002) added a gradient diffusion term to the viscoelastic model to construct a viscoelastic–diffusion model for oscillatory turbulent boundary layers. The resulting analytical solutions demonstrated improvement over the eddy viscosity model in predicting the observed temporal evolution and vertical structure of the velocity and shear stress profiles observed by Jonsson and Carlson (1976), van Doorn (1982), Sleath (1987), and Jensen et al. (1989).

Studies of bottom sloping effects on wave bottom boundary layers, either theoretical or observational, are lacking. Chu and Mei (1970) developed a potential flow theory for the evolution of a Stokes wave train over a mild slope, finding that the local bottom slope causes wave phase to be dependent on the vertical coordinate. Thus, while the horizontal and vertical velocities are in quadrature in the interior flow for a horizontal bottom, this is no longer the case for a sloping bottom when a perturbation to the vertical velocity is induced that is in phase with the horizontal velocity (cf. Zou and Hay 2001; Zou et al. 2003). To study the influence of bottom slope on fluid mass transport, Bijker et al. (1974) obtained solutions for the oscillatory boundary layer over a sloping bottom for a laminar case.

Trowbridge and Agrawal (1995) carried out the first comprehensive comparison between field measurements of the vertical structure of the WBL and theory. The measurements were made using a laser Doppler velocimeter, displaced mechanically to obtain measurements at different heights. Foster (1996) used a five-element array of hot films at centimeter spacing to resolve the WBL. More recently, Smyth et al. (2002) and Smyth and Hay (2002) have used a pulse-coherent centimeter resolution acoustic Doppler profiling instrument developed by Zedel and Hay (1999) to obtain the vertical turbulence intensity through the WBL to the bed. Advantages of the Doppler profiling technique includes that the measurement being made remotely with minimal disturbance to the near-bed flow, that the positions of the measurement points relative to the bed can be determined from the backscatter profile, and that the profiles are acquired synoptically.

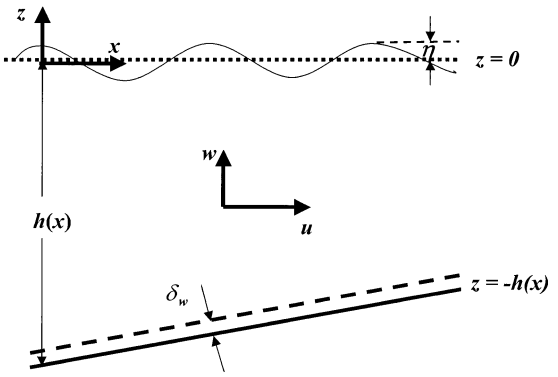

FIG. 1. Definition sketch showing variables and coordinate system for waves propagating over a planar, sloping seabed.

Our primary objectives in this paper are to construct solutions for the turbulent WBL under irregular (i.e., nonmonochromatic) waves above a sloping bottom and to compare the predicted velocity and shear stress fields to field measurements made using the coherent Doppler profiler. The model–data comparisons also yield estimates of equivalent bottom roughness and friction velocity, which are compared to the values obtained from the momentum integral method and from the nearbed turbulence intensity and with Nielsen's (1992) and Tolman's (1994) semiempirical formulation.

The paper is presented in the following order. The theory for the wave turbulent boundary layer over a sloping bed is derived in section 2, followed by brief descriptions of the field observations and instrumentation in section 3. The field measurements are analyzed and compared with theory in section 4. These results and their implications, particularly regarding the bed shear stress, are discussed further in section 5. Last, the major findings of this study are summarized in section 6.

2. Theory

We consider here the wave turbulent boundary layer over a sloping bed. Figure 1 shows the coordinate system and primary variables. The fluid density ρ is set to unity, and so does not explicitly appear in the equations hereinafter.

a. The viscoelastic model

From his analysis of Jonsson and Carlsen's (1976) experiment, Nielsen (1984) observed a phase shift be-

tween shear stress and velocity gradient that varies with the height above the bed and suggested that either a time-variant real eddy viscosity or a complex eddy viscosity be adapted to explain such behavior. Neilsen also pointed out the lack of theoretical basis for the complex eddy viscosity. As shown by Zou (2002), including a turbulent relaxation term to the conventional eddy viscosity model leads to a complex eddy viscosity.

To include eddy relaxation and diffusion effects in oscillatory flow boundary layers, Zou (2002) used Townsend's (1972) turbulent energy equation to obtain (cf. Zou 1998)

$$T_e\frac{D\tau}{Dt} + \tau = \nu_0(u_z + w_x) + T_e(\nu_0\tau_z)_z, \quad (2.1)$$

where the subscripts x and z signify partial differentiation, τ is the shear stress, ν_0 is an eddy diffusivity, $z + h$ is the height above the bed, $\kappa \approx 0.4$ is the von Kármán constant, and u_* is the friction velocity and is equal to the square root of the bed shear stress amplitude.

The first term on the left in Eq. (2.1) represents eddy relaxation, with T_e being an eddy relaxation timescale. The second term on the right represents gradient diffusion. In the absence of eddy relaxation and diffusion, (2.1) reduces to $\tau = \tau_e = \nu_0(u_z + w_x)$, which is the conventional eddy viscosity representation of shear stress. An assumption underlying (2.1) is that the ratio between shear stress $-\langle u'w'\rangle$ and the turbulent kinetic energy q^2 is a constant. For steady flow, the empirical value of this constant, $a_1 = -\langle u'w'\rangle/q^2$, is $a_1 = O(\kappa^2)$ (cf. Townsend 1972, 1976). The eddy relaxation time is given by the ratio between the eddy velocity and length scales and involves a_1; that is, $T_e(z) = l_e/(a_1u_*)$, where $l_e = \kappa(z + h)$ is the eddy mixing length and u_* is the eddy velocity scale.

For a wave turbulent boundary layer beneath a monochromatic wave with radian frequency ω, the viscoelastic model [the first three terms of (2.1)] leads to a complex effective eddy viscosity

$$\nu = \nu_0(z)\Big/\left(1 + i\alpha\frac{z + h}{l}\right) = \frac{\nu_0(z)}{1 + i\omega T_e(z)}, \quad (2.2)$$

where $\nu_0 = \kappa u_*(z + h)$, $\alpha = \kappa^2/a_1$ is the eddy relaxation coefficient and, following Zou (2002), is set equal to 2 here, and $l = \kappa u_*/\omega$ is the wave boundary layer thickness according to Grant and Madsen (1986).

It can be seen from Equation (2.1) that at $z + h \sim l$, $\omega T_e \sim \alpha$, therefore, the relaxation and diffusion terms become $T_e(D\tau/Dt) \sim \alpha\tau$ and $T_e(\nu_0\tau_z)_z \sim \alpha\tau$. Thus, in the upper region of WBL, both the eddy relaxation diffusion terms must be retained in the turbulent energy balance.

b. Monochromatic waves

For a monochromatic progressive wave, the horizontal wave orbital velocity is

$$u_b = \hat{u}_b e^{i(\omega t - kx)} + \text{c.c.}, \quad (2.3)$$

where $\hat{u}_b = a\omega$, a is the excursion amplitude of the wave orbital motion, k is the wavenumber, and c.c. denotes the complex conjugate of the preceding term and will be omitted hereinafter. The x component of the Reynolds-averaged Navier–Stokes equations for the boundary layer is

$$\frac{\partial u}{\partial t} = \frac{\partial u_b}{\partial t} + \tau_z, \quad (2.4)$$

where τ is the shear stress related to the velocity strain by the turbulent closure model (2.1).

The boundary conditions follow from no-slip and no normal flow conditions at the bottom and continuity of velocity at the top of the boundary layer; that is,

$$u = w = 0 \quad \text{at } z + h \to z_0, \quad \text{and} \quad (2.5)$$

$$u = u_b \qquad \text{at } z = z_b \quad (2.6)$$

where $z_0 = r/30$, r is the bed roughness (see appendix A), and z_b is a reference depth near the bed but outside the WBL.

The governing equation (2.4) for the horizontal velocity within the turbulent boundary layer is a first-order approximation assuming a small wave steepness and a boundary layer thickness much smaller than the wavelength, and is the same as that for the WBL over a horizontal bottom, as are the boundary conditions. Therefore, through the boundary layer, the vertical transformation of horizontal velocity relative to the wave bottom orbital velocity above the WBL, u_b, can be taken as the same as that in the horizontal bottom cases. The dependence of u on bottom slope arises through u_b, which is obtained by Zou et al. (2003) based on the Chu and Mei (1970) theory and is affected by the bottom slope.

The bottom slope has a first-order effect on the vertical velocity in the lower portion of the interior flow (Zou et al. 2003). A similar first-order effect is expected in the WBL, which can be evaluated by substituting the horizontal velocity solutions given by Zou (2002) for the WBL and the boundary condition (2.5) into the mass conservation equation

$$u_x + w_z = 0 \quad (2.7)$$

and integrating over $(-h, z)$; that is,

$$w = -\int_{-h} u_x\, dz = ik\left(1 + i\frac{\hat{u}_{bx}}{k\hat{u}_b}\right)\int_{-h}^{z} u\, dz - h_x u, \quad (2.8)$$

where h is the water depth, and $\hat{u}_{bx}/\hat{u}_b$ is the relative amplitude change of waves shoaling over a slope. (2.8) may be rewritten as

$$w = \left(1 + i\frac{\hat{u}_{bx}}{k\hat{u}_b}\right)w_{\text{horiz}} - h_x u, \tag{2.9}$$

where

$$w_{\text{horiz}} = ik\left[\int_{-h}^{z} u_b\, dz + \frac{1}{i\omega}(\tau - \tau_0)\right] \tag{2.10}$$

is the corresponding vertical velocity for a horizontal bottom and τ_0 is the shear stress at the bed.

According to (2.9), in the presence of bottom slope, the vertical velocity is composed of three parts: w_{horiz}, the vertical velocity for a horizontal bottom; $i(k\hat{u}_b)^{-1}\hat{u}_{bx}w_{\text{horiz}}$, due to wave shoaling; and $h_x u$, due to the depth change. The last two parts are both proportional to the magnitude of the bed slope and are 90° out of phase with w_{horiz}. The terms involving bottom slope are at order $O(h_x u)$ while $w_{\text{horiz}} \sim k(z + h)u_b$; therefore, at $z + h \sim k^{-1}h_x|u/u_b|$, bottom slope has a first-order effect on w and at $z + h \ll k^{-1}h_x|u/u_b|$, the bottom slope effects dominate and the vertical velocity reduces to $w \approx -h_x u$. It follows that only if $\delta_w \ll k^{-1}h_x$ may the vertical velocity solution be approximated by $-h_x u$ through the WBL.

c. The WBL solutions

From the viscoelastic–diffusion model (Zou 2002), the (complex valued) transfer function between the horizontal velocity u within the WBL and the wave bottom orbital velocity u_b at a the reference height $z_b + h$ well outside the WBL is

$$H_{uu_b}(\omega, z) = 1 - \frac{F_1(\alpha, \zeta)}{F_1(\alpha, \zeta_0)}, \tag{2.11}$$

where

$$F_1(\alpha, \zeta) = (1 + i\alpha\zeta)^{-1/2}\left[\frac{\text{ker}2\sqrt{\zeta} + i\,\text{kei}2\sqrt{\zeta}}{\text{ker}2\sqrt{\zeta_0} + i\,\text{kei}2\sqrt{\zeta_0}} + \frac{\alpha}{2}\sqrt{i\zeta}\,\frac{\text{ker}_1 2\sqrt{\zeta} + i\,\text{kei}_1 2\sqrt{\zeta}}{\text{ker}2\sqrt{\zeta_0} + i\,\text{kei}2\sqrt{\zeta_0}}(1 + i\alpha\zeta)^{-1}\right], \tag{2.12}$$

$\zeta = \omega(z + h)/(\kappa u_*)$, $\zeta_0 = \omega z_0/(\kappa u_*)$, and (ker, kei) and ($\text{ker}_1$, kei_1) are the zero- and first-order Kelvin functions (Abramowitz and Stegun 1970). The standard eddy viscosity solution is recovered by setting α to zero (Zou 2002). Thus, the effect of the complex eddy viscosity [Eq. (2.2)] is to introduce additional imaginary terms that alter the predicted vertical structure of u, in both magnitude and phase but especially the phase.

Combining (2.9) with the vertical velocity and shear stress solutions by Zou (2002) yields the (complex valued) transfer function between the vertical velocity w and u_b

$$H_{wu_b}(\omega, z) = \left(1 - \frac{\hat{u}_{bx}}{ik\hat{u}_b}\right)H_{wu_b}(\omega, z)|_{\text{horiz}} - h_x H_{uu_b}(\omega, z), \tag{2.13}$$

where

$$H_{wu_b}(\omega, z)|_{\text{horiz}} = ik\{(z + h) + (i\omega)^{-1}[H_{\tau u_b}(\omega, z) - H_{\tau u_b}(\omega, z_0 - h)]\}, \tag{2.14}$$

and between the stress τ and u_b

$$H_{\tau u_b}(f, z) = \kappa[F_1(\alpha, \zeta_0)]^{-1}(1 + i\alpha\zeta)^{-1/2} \times \sqrt{i\zeta}\,\frac{\text{ker}_1 2\sqrt{\zeta} + i\,\text{kei}_1 2\sqrt{\zeta}}{\text{ker}2\sqrt{\zeta_0} + i\,\text{kei}2\sqrt{\zeta_0}}. \tag{2.15}$$

The transfer functions between horizontal and vertical velocities (u, w), and surface elevation η are

$$H_{u\eta}(\omega, z) = H_{u_b\eta}(\omega)H_{uu_b}(\omega, z), \quad \text{and} \tag{2.16}$$

$$H_{w\eta}(\omega, z) = H_{u_b\eta}(\omega)H_{wu_b}(\omega, z), \tag{2.17}$$

where $H_{u_b\eta}(\omega)$ is the transfer function between u_b and η obtained from the Chu and Mei (1970) velocity potential solution (Zou et al. 2003).

Figure 2 demonstrates how the bed slope affects the vertical profiles of $H_{u\eta}(\omega, z)$ and $H_{w\eta}(\omega, z)$ at a frequency of 0.12 Hz given a roughness length of 1.08 cm and friction velocity of 4.8 cm s^{-1}. The velocity profiles predicted using the present theory (2.11) and (2.13) are indicated by the solid lines; those using Chu and Mei's (1970) potential wave theory by the dashed lines. Both solutions exhibit significant sloping bed effects on the magnitude and phase of the vertical velocity and the phase of the horizontal velocity, but negligible changes to the magnitude of the horizontal velocity. The two sloping bottom solutions differ only in the WBL region where bottom friction becomes significant. While the present theory predicts overshooting in the magnitude of the horizontal velocity regardless of bottom slope, overshooting in the magnitude of the vertical velocity is predicted only in the presence of a sloping bed. Overshoot in the magnitude of u is due to turbulent friction, therefore, is not present in the potential theory results. The overshoot in the magnitude and phase of w predicted for the sloping bed comes from the bottom-slope-induced component $h_x u$ in (2.9) as discussed in section 2b.

We also note that the sloping bottom effect on vertical velocity decreases with increasing height above the bed

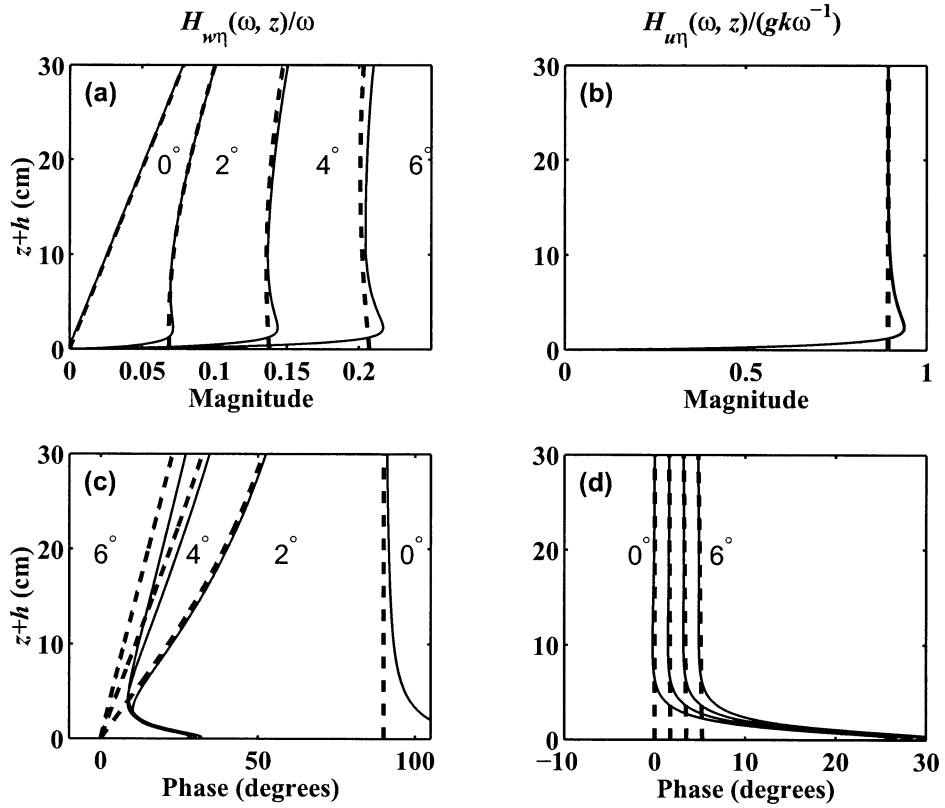

FIG. 2. Predicted vertical profiles of the magnitude and phase of the normalized transfer functions $H_{w\eta}/\omega$ and $H_{u\eta}/(gk\omega^{-1})$ between velocity components, u or w, and surface elevation η at frequency $f = 0.12$ Hz and water depth $h = 3.67$ m: the present theory (solid lines) with bottom roughness length $r = 1.08$ cm and friction velocity $u_* = 4.8$ cm s^{-1}; Chu and Mei (1970) theory (dashed lines). Predictions are shown for bed slopes of 0°, 2°, 4°, and 6°.

so that the significant bottom effect is confined to the lower water column, but extends far above the WBL. The thickness of this region increases with slope and decreases with frequency for a given water depth (cf. Zou and Hay 2001). The vertical velocity is in phase with the horizontal velocity at the bed and approaches 90° out of phase with the horizontal velocity far away from the bed [but does not achieve exact quadrature, even at the surface (Zou et al. 2003)].

3. Field experiment and data analysis

The field measurements used here for comparison with theory were carried out at Queensland Beach, Nova Scotia, an *O*(100 m)-long, unbarred, pocket beach facing a narrow opening to the sea so that waves propagating to the beach from the continental shelf tend to be unidirectional and normally incident and the longshore currents are small. The measurements were collected at a location approximately 60 m from the shoreline, in a mean water depth of 3.7 m where the local bed slope was about 2°, and seabed sediments were composed of fine sand with a median diameter of 0.17 mm. Vertical and horizontal velocity profiles with 0.7 cm vertical resolution were acquired with a bistatic coherent Doppler profiler (CDP: see Zedel and Hay 1999, 2002) at a profile acquisition rate of about 30 Hz, using nine pulse-pair averaging. Surface elevation was measured at 30-min intervals with an upward-looking, pencil-beam acoustic sounder at a sampling rate of 8 Hz. Bedform geometry was detected at 30-min intervals by cm-resolution rotary sidescan and pencil beam sonars (Hay and Wilson 1994; Ngusaru and Hay 2003), and continuously except during daylight with a millimeter resolution laser–video system (Crawford and Hay 1999). The reader is referred to Crawford and Hay (2001) and Smyth et al. (2002) for more detailed descriptions of the experiment and field site.

A single storm event was captured during the course of the 11-day experiment. During this storm, a variety of bedform types were observed, including flat bed at the height of the storm and, immediately preceding and immediately following the occurrence of flat bed, linear transition ripples (Dingler and Inman 1976; Crawford and Hay 2001). Power spectra of the surface elevation $S_{\eta\eta}$ are shown for the flat bed period and the linear transition ripple period in Fig. 3. The wave spectra during the flat bed period are noticeably bimodal and nonstationary; those

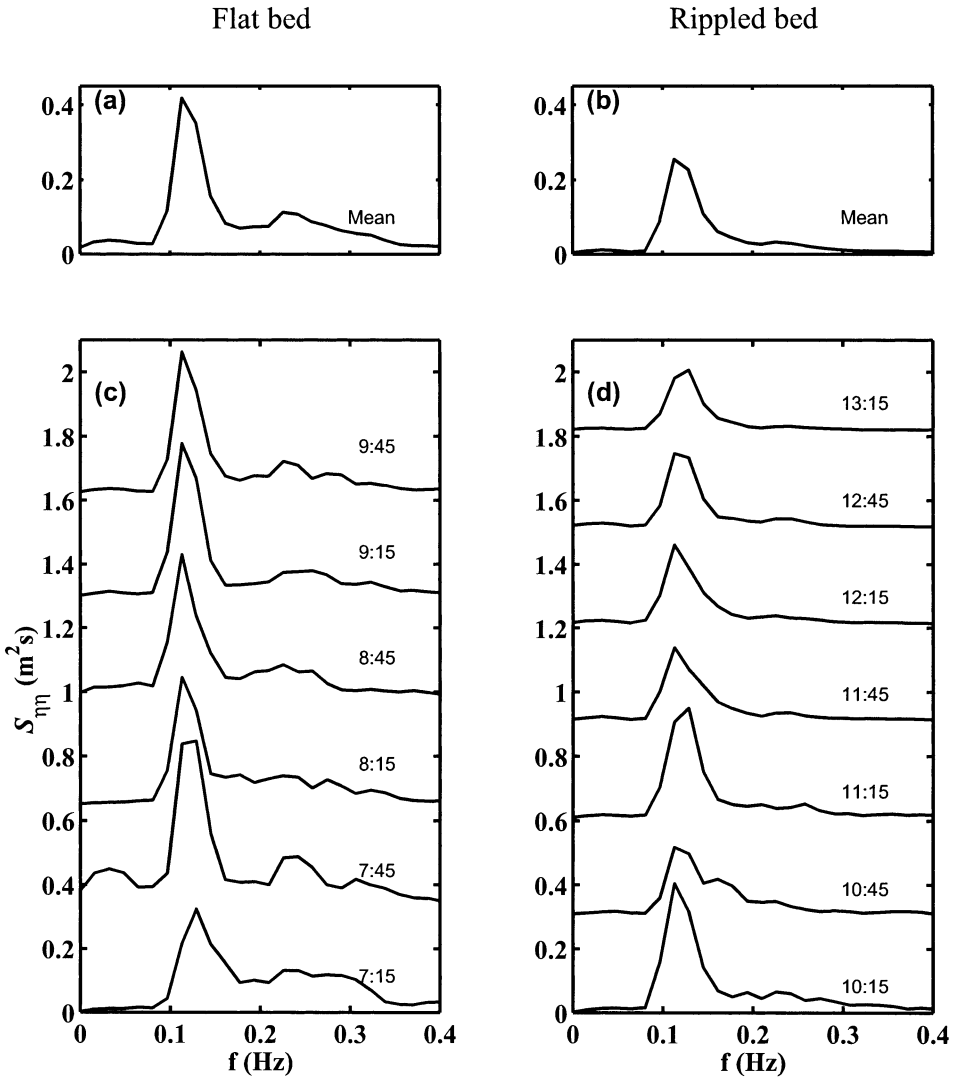

FIG. 3. Surface elevation spectra, $S_{\eta\eta}$: (a),(c) flat bed interval and (b),(d) linear transitional ripple intervals. Panels (a) and (b) are the ensemble average over all runs in each interval; (c) and (d) show the spectra for each of 8-min data run, labeled with the starting time in UTC.

during the linear transition ripple period are more unimodal and more nearly stationary. As discussed by Crawford and Hay (2001), these differences are due to the evolution of the wave field from a mix of sea and swell as the wave forcing approached its peak to a residual swell spectrum as the storm event decayed.

Near-bed velocity profiles were measured with the CDP extending through the WBL to the bed. The CDP transceivers were mounted on a cantilevered frame (see Smyth et al. 2002) at a nominal height of 80 cm above the bed. The vertical velocity profiles extended to a height of about 50 cm from the bed; the horizontal velocity profiles to a height of about 30 cm. The expected accuracy of the vertical and horizontal velocities in each nine pulse-pair averaged profile is about 0.17 and 0.7 cm s^{-1}, respectively (cf. Zedel and Hay 1999). Each CDP data run was 8-min duration. Two runs were acquired every 30 min.

The wave parameters and the grain roughness Shields parameter for the flat bed and rippled bed intervals are given in Table 1. The linear transition ripples were 3 mm high with 8.5 cm wave length and migrated toward

TABLE 1. Mean wave peak frequency f_p, wavenumber k_p, water depth h, significant wave height H_s, u_{rms} at height 20 cm above bottom, and the grain roughness Shields parameter $\theta_{2.5}$ (see appendix A), estimated using the significant wave orbital velocity.

Bed state	f_p (Hz)	k_p (m^{-1})	h (m)	H_s (m)	u_{rms} (m s^{-1})	$\theta_{2.5}$
Flat	0.12	0.13	3.7	1.1	0.36	0.6–0.8
Rippled	0.12	0.15	3.1	0.74	0.30	0.3–0.4

shore at 0.3 cm min^{-1} (Crawford and Hay 2001). Thus, ripple height was much less than the expected WBL thickness δ_w, ripple wavelength 0.05–0.25 times the value of the significant wave orbital excursion, so that they represented roughness elements to the interior flow, and the ensemble-averaged CDP measurements may be taken as the equivalent of spatial averages over several ripple wavelengths.

Power spectra S_{uu}, S_{ww}, and $S_{\eta\eta}$ of the velocity components (u, w) and surface elevation η and the cross-spectra $C_{u\eta}$ and $C_{w\eta}$ were estimated using Welch's averaged periodogram method and a Hanning window, dividing each 8-min data run into demeaned and detrended 2048-sample segments overlapped by 75%. The surface elevation measurements were interpolated to the CDP profile time base prior to computing the cross-spectra. Degrees of freedom n_d are 140 and 164 for the ensemble spectra of flat and rippled bed cases. Transfer functions were obtained from the auto- and cross-spectra according to

$$H_{u\eta}(\omega, z) = \frac{C_{u\eta}(\omega, z)}{S_{\eta\eta}(\omega)}, \tag{3.1}$$

$$H_{w\eta}(\omega, z) = \frac{C_{w\eta}(\omega, z)}{S_{\eta\eta}(\omega)}. \tag{3.2}$$

A similar method was implemented to obtain the transfer functions between components (u, w) and the wave bottom velocity u_b at 20 cm above the bed, that is

$$H_{uu_b}(\omega, z) = \frac{C_{uu_b}(\omega, z)}{S_{u_bu_b}(\omega)}, \tag{3.3}$$

$$H_{wu_b}(\omega, z) = \frac{C_{wu_b}(\omega, z)}{S_{u_bu_b}(\omega)}. \tag{3.4}$$

Confidence intervals (95%) for the transfer functions are estimated using the relationship (Bendat and Piersol 1986, section 9.2.4).

$$\overline{|H|}(1 - 2\varepsilon) \le |H| \le \overline{|H|}(1 + 2\varepsilon), \tag{3.5}$$

where $\overline{|H|}$ and $|H|$ are the estimated and expected values for the magnitude of the transfer functions, the subscripts ($u\eta$) and ($w\eta$) are omitted here, and ε is the normalized random error

$$\varepsilon = \frac{[1 - \gamma^2(\omega)]^{1/2}}{|\gamma(\omega)|\sqrt{2n_d}}, \tag{3.6}$$

where $\gamma^2(\omega)$ is the corresponding estimated coherence. According to Bendat and Piersol, the standard deviation of the transfer function phase measured in radians is approximately equal to the normalized random error of the transfer function magnitude. The coherence functions between (u, w) and η are

$$\gamma^2_{u\eta}(\omega, z) = \frac{|C_{u\eta}(\omega, z)|^2}{S_{uu}(\omega)S_{\eta\eta}(\omega)}, \tag{3.7}$$

$$\gamma^2_{w\eta}(\omega, z) = \frac{|C_{w\eta}(\omega, z)|^2}{S_{ww}(\omega)S_{\eta\eta}(\omega)}. \tag{3.8}$$

Figure 4 shows the profiles of γ^2 at the wave peak frequency ω_p and $2\omega_p$.

For the flat bed interval, $\gamma^2_{u\eta}$ remains constant at about 0.95 for heights greater than 2.5 cm above the bed (Fig. 4b) and decreases toward the bed below 2.5-cm height, at both the peak and double peak frequency. In comparison, the profiles of $\gamma^2_{w\eta}$ are more irregular, and exhibit lower coherence except in the 2 or 3 bins just above the bed (Fig. 4a). At the peak frequency, $\gamma^2_{w\eta}$ increases from 0.8 to 0.85 in the bin immediately above the bed. At $2\omega_p$, $\gamma^2_{w\eta}$ increases from 0.65 to 0.8 just above the bed.

For the rippled bed interval, the $\gamma^2_{u\eta}$ profiles are similar to their flat bed counterparts except for the overall lower coherences at $2\omega_p$ (Fig. 4d). The $\gamma^2_{w\eta}$ profile at the peak frequency is also somewhat similar to the flat bed case (although coherences are higher and more uniform with height) and, as with the u component, the coherences at $2\omega_p$ are significantly lower (Fig. 4c).

Thus for the rippled bed interval, $\gamma^2_{w\eta}$ at $2\omega_p$ is only about half that for flat bed. The reasons are the following: the wave harmonic component decreases in magnitude by a factor of 2–4 (cf. Fig. 3); and the ratio of turbulent to wave energy increases during rippled bed interval.

The depth dependence of $\gamma^2_{u\eta}$ is much weaker than that of $\gamma^2_{w\eta}$, particularly at $2\omega_p$. Turbulence intensity increases toward the bed, reducing the coherence between the wave-band velocities and surface elevation. At a fixed point above the bed, the ratio of turbulent to wave energy increases with frequency. These two processes give rise to the depth- and frequency-dependent behavior of $\gamma^2_{w\eta}(\omega, z)$. In addition, the horizontal velocity component is not well-resolved by the CDP in the 3–4 bins adjacent to the bed because the slanting acoustic beams used to separate the vertical and horizontal velocities are contaminated by the bottom reflection (see Zedel and Hay 2002). This is the primary cause of the reduced $\gamma^2_{u\eta}$ values in the 3 bins immediately above bottom in Figs. 4b and 4d. Thus, u at the three near-bed points have been inferred from the near-bed vertical velocity using the relationship $u \sim -w/h_x$ (cf. section 2b), and are identified by different symbols.

The CDP has a vertical resolution of 0.7 cm, so the bed elevation can vary by as much as 0.35 cm without changing its apparent position (i.e., without changing the range bin in which the bottom echo appears). Neither u nor w as estimated by CDP necessarily goes to zero at the measurement point closest to the bed. Assuming that the vertical velocity vanishes at $z + h = z_0$, we extrapolate the last two vertical velocity measurements

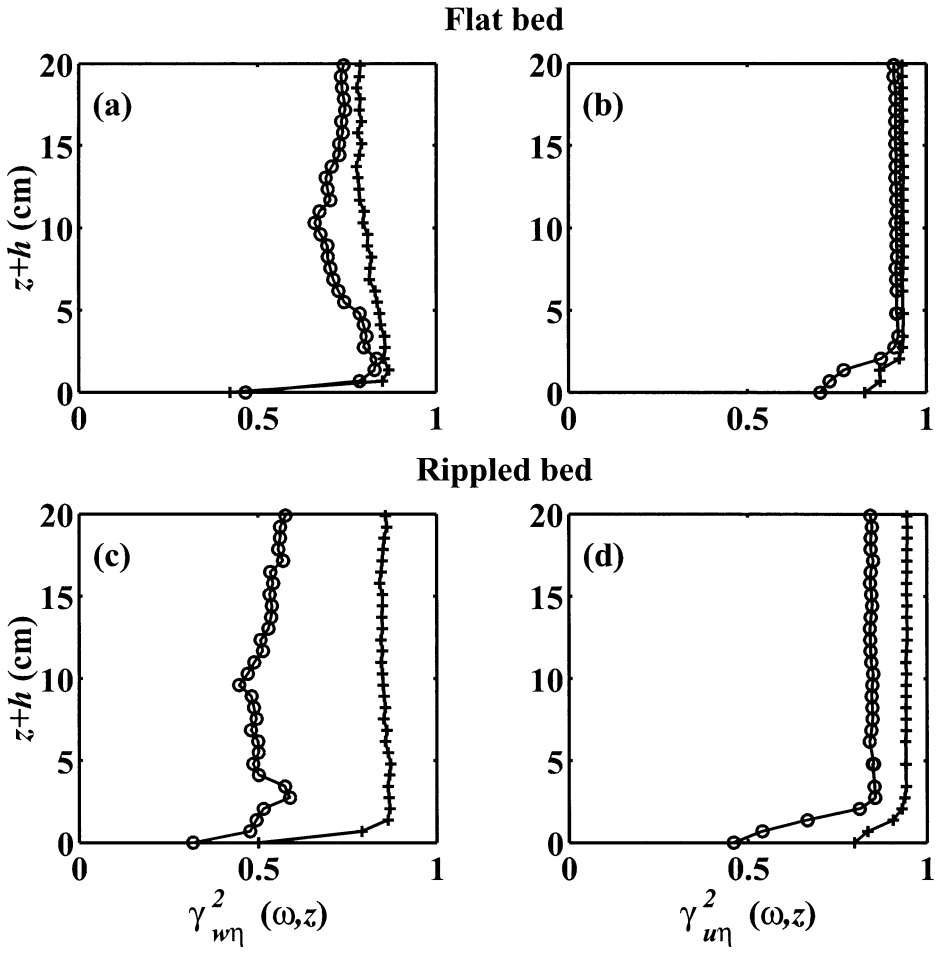

FIG. 4. Profiles of the coherence functions, $\gamma^2_{w\eta}$ and $\gamma^2_{u\eta}$, between the observed u and w, and the observed surface elevation η at the wave peak (+) and double peak frequencies (○) for (a),(b) the flat bed interval and (c),(d) the rippled bed interval.

linearly to zero to give a new estimate of the bed location.

4. Comparison of theory and field measurements

We use the reference height $z_b + h = 20$ cm above the bed to define the wave bottom orbital velocity outside the WBL, that is,

$$u_b = u|_{z=z_b}. \tag{4.1}$$

This is the height farthest above the bed at which CDP gives reliable measurements of the horizontal velocities. According to the observed velocity profiles shown later, the WBL extends to about 7 cm above the bed at the wave peak frequency. Thus, this reference height is several times as great as the WBL thickness.

a. Bottom roughness

To compare the present WBL solutions with field measurements, an estimate of roughness length is needed. We determine the roughness length $z_0 = r/30$ by optimizing the model predictions relative to the observed velocity profiles in a least squares sense, using the following depth-averaged velocity discrepancy functions

$$\Delta_u(\omega, z_u) = \frac{\int_0^{z_u} |H^{\text{pred}}_{uu_b}(\omega, z) - H^{\text{obs}}_{uu_b}(\omega, z)|^2\, dz}{\int_0^{z_u} |H^{\text{obs}}_{uu_b}(\omega, z)|^2\, dz}, \tag{4.2}$$

$$\Delta_w(\omega, z_u) = \frac{\int_0^{z_u} |H^{\text{pred}}_{wu_b}(\omega, z) - H^{\text{obs}}_{wu_b}(\omega, z)|^2\, dz}{\int_0^{z_u} |H^{\text{obs}}_{wu_b}(\omega, z)|^2\, dz}, \tag{4.3}$$

and

$$\Delta(\omega, z_u) = \frac{1}{2}[\Delta_u(\omega, z_u) + \Delta_w(\omega, z_u)], \tag{4.4}$$

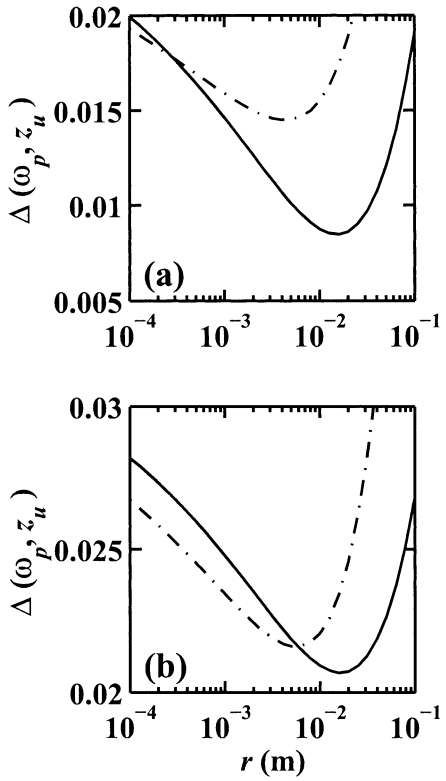

FIG. 5. Depth-averaged normalized discrepancy function $\Delta(\omega_p, z_u)$ between observed and predicted velocity transfer functions (integrated over the WBL) at the wave peak frequency for z_u set to 10 cm above the bed during (a) the flat bed interval and (b) the rippled bed interval. Viscoelastic–diffusion model indicated by solid lines; standard eddy viscosity model shown by dash–dot lines.

where $\Delta(\omega, z_u)$ represents the relative discrepancy between predicted and measured velocity integrated over a depth interval of z_u.

The discrepancy functions are plotted in Fig. 5 as a function of the bottom roughness r, at the peak frequency for the flat and rippled bed intervals, and for both viscoelastic–diffusion and eddy viscosity models. The discrepancy functions each exhibit a minimum value at a particular roughness $r = r_m$. For the flat bed interval (Fig. 5a), the viscoelastic–diffusion model gives rise to a relative error one-half that of eddy viscosity model, at $r = r_m$. In addition, the discrepancy function for the viscoelastic model displays higher curvature near the minimum and is therefore more robust in resolving the roughness value by optimizing the model–data comparisons. The improvement of the viscoelastic–diffusion model over the standard eddy viscosity model in predicting the observed velocity profile is less obvious for the rippled bed interval (Fig. 5b). The hydraulic roughnesses obtained from these r_m values are later compared with the measured physical roughness of the bed. Here r_m is used to specify z_0 and the representative friction velocity u_* for irregular waves is then determined as outlined in appendix B. Assuming a linear vertical transformation of velocities through the WBL, the same bottom roughness and friction velocity is applied to the WBL solutions (2.11) and (2.13) for each Fourier component (Madsen and Wikramanayake 1991; Beach and Sternberg 1992; Mathisen and Madsen 1999; appendix B).

b. Velocities

1) FLAT BED INTERVAL

Predicted near-bed velocity power spectra were obtained by substituting the measured surface elevation spectra $S_{\eta\eta}(\omega)$ over a frequency range from 0.05 to 0.5 Hz in the WBL solutions for each Fourier component:

$$S_{ww}(\omega, z) = |H_{w\eta}(\omega, z)|^2 S_{\eta\eta}(\omega), \quad (4.5)$$

$$S_{uu}(\omega, z) = |H_{u\eta}(\omega, z)|^2 S_{\eta\eta}(\omega). \quad (4.6)$$

Figure 6 shows the predicted and observed spectra at heights of 2, 3, 5, and 10 cm above the bed for the incident wave band, 0.05–0.5 Hz. The S_{ww} predictions with slope are in good agreement with the measurements, whereas those without slope are much too low, and the deficit increases rapidly toward the bed. The S_{uu} predictions with and without slope are identical and in reasonably good agreement with the measurements, except very close to the bed where (i.e., at height 2 cm) the horizontal velocity measurements are less accurate because of contamination of the near-bottom bins of the CDP's inclined acoustic beams by the bottom reflection (Zedel and Hay 2002). At heights greater than 2 cm, the theory slightly overpredicts the observed S_{uu}: this difference is likely due to that fraction of the total wave-band velocity variance associated with directional spreading in the incident waves, which is not included in the observations since the v component was not measured, but is included in the predictions since they are based on the observed sea surface elevations.

The sloping bottom theory is consistent with the observations, particularly at heights of 3 and 5 cm, which are well within the WBL (as shown later, and for which S_{uu} is uncontaminated by the bottom reflection), indicates that bottom friction effects on each Fourier component are well represented by a single equivalent roughness length and friction velocity. Linear theory appears to adequately describe the transfer function between the surface elevation and the near-bed velocities within the WBL, not only at the peak frequencies but also at their harmonics. This finding is similar to that for the interior flow by Zou et al. (2003).

Figure 7 shows the predicted and observed magnitudes of the transfer functions $|H_{wu_b}|$ and $|H_{uu_b}|$ between (u, w) and the free stream velocity, u_b, as functions of frequency at 3 and 7 cm above the bed for the flat bed interval. The observed values of $|H_{wu_b}|$ (denoted by plus signs) are consistent with the predictions for a sloping bottom (solid lines), but deviate signifi-

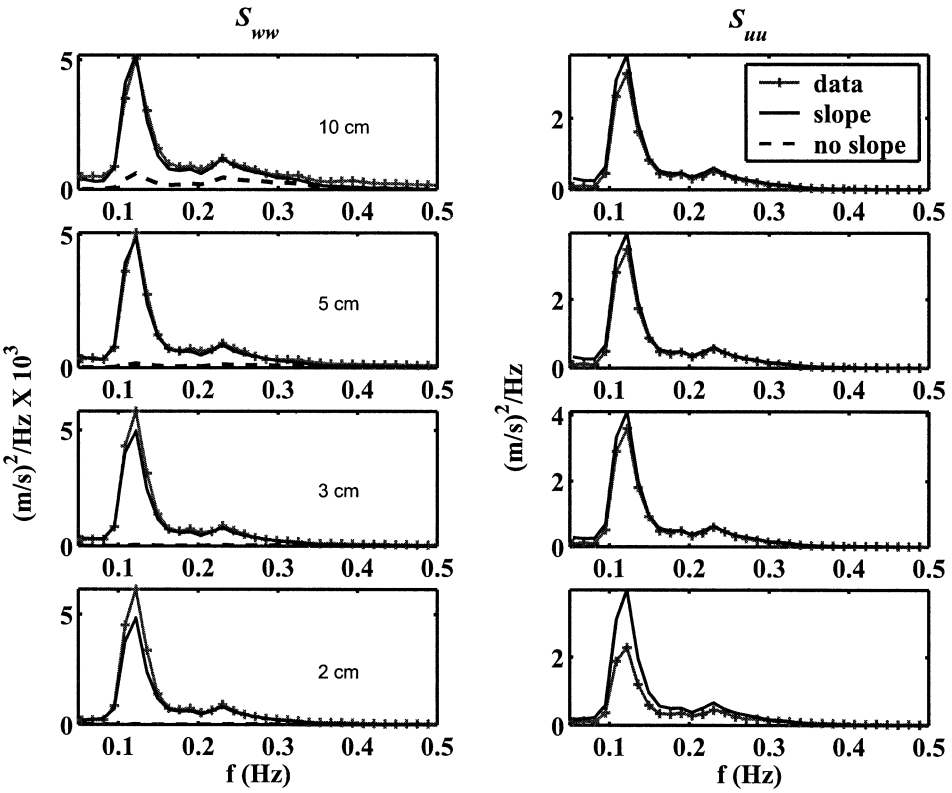

FIG. 6. Velocity spectra at heights of 2, 3, 5, and 10 cm above bottom for the flat bed interval predicted for $h_x = 2°$ (solid lines) and $h_x = 0°$ (dashed lines) and observed (+). Predictions are based on the measured surface elevation spectra and the present theory; (left) vertical velocity spectra S_{ww} and (right) horizontal velocity spectra S_{uu}.

cantly from those for a horizontal bottom (dashed lines). It is also evident that the deviation between the predicted $|H_{wu_b}|$ with and without bottom slope increases with decreasing frequency as well as with decreasing height above the bed. The predictions and observations of $|H_{uu_b}|$ compare well regardless of the bottom slope.

Similar comparisons are carried out in Fig. 8 for the transfer function phase. The observed frequency-dependence of the phase of H_{wu_b} is highly consistent with the sloping bottom predictions (solid lines). The predicted phases for a horizontal bottom (dashed lines) are clearly inconsistent with the measurements. The deviation between the predicted phase of H_{wu_b}, with and without bottom slope, increases with decreasing frequency and decreasing height above the bed. The predicted phase of H_{wu_b} without bottom slope increases above 90° toward lower frequencies, and at a faster rate closer to the bed, due to turbulent friction in the WBL. A similar tendency can be seen in the curvature of the predicted sloping bed phases. The observed phase of H_{uu_b} (denoted by plus signs) are consistent with the predictions regardless of bottom slope. These results indicate that horizontal and vertical velocities are not in quadrature in the presence of a sloping bed and that the phase difference within the WBL is dependent on frequency as well as height above the bed.

Vertical profiles of the magnitude and phase of H_{wu_b} and H_{uu_b} at the wave peak frequency ω_p and double peak frequency $2\omega_p$ are shown in Fig. 9. While the horizontal-bed inviscid predictions for H_{wu_b} are clearly incorrect (Figs. 9a and 9c), both WBL models including bottom slope result in profiles which are generally consistent with the measurements. The agreement with the viscoelastic model profiles is better, particularly in the bottom 3–5 cm. The predicted magnitude and phase profiles for H_{uu_b} using the viscoelastic WBL model are also in better agreement with the observations than the standard eddy viscosity model (Figs. 9b and 9d). Note that the predicted phase change of H_{uu_b} by the standard eddy viscosity model begins much farther from the bed than that by the viscoelastic model and from the observations.

2) RIPPLED BED INTERVAL

The same comparisons as in the preceding subsection are presented for the rippled bed interval in Figs. 10–13. Overall, the transfer function results are very similar to those for the flat bed interval (cf. Fig. 9 with 7, Fig. 10 with 8, and Fig. 13 with 9). Also as before, the vertical velocity power spectral densities (Fig. 10) are underpredicted by the horizontal bed theory. Unlike the

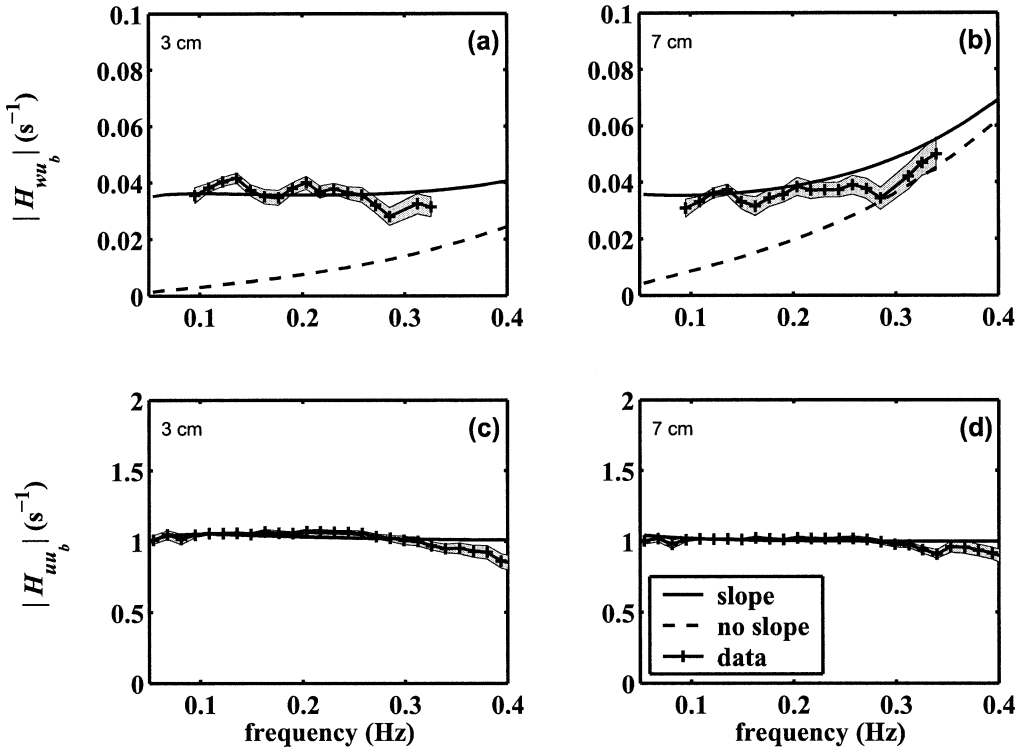

FIG. 7. Predicted and observed magnitudes of the transfer functions H_{wu_b} and H_{uu_b} vs frequency at 3 and 7 cm above the bed for the flat bed interval: (a),(b) $|H_{wu_b}|$ and (c),(d) $|H_{uu_b}|$. The predictions are for 0° bed slope (dashed lines) and 2° (solid lines). Observed values (+) with coherences between u or w and u_b larger than 0.5 are shown. Gray shading represents the 95% confidence interval.

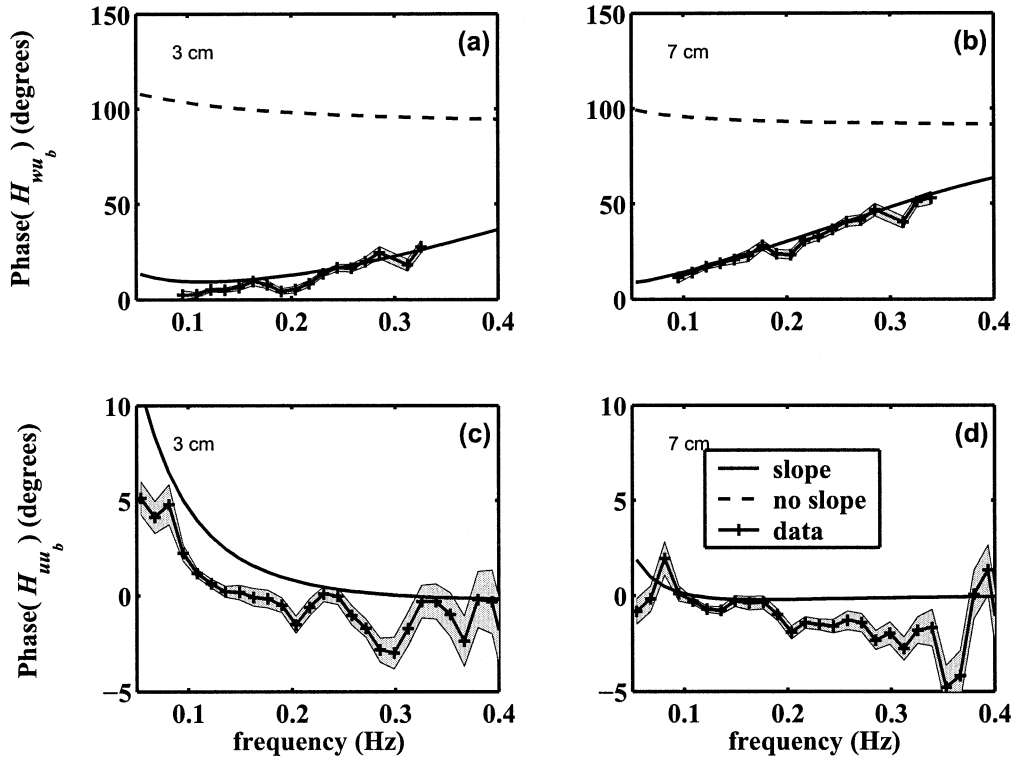

FIG. 8. Predicted and observed phases of the transfer functions H_{wu_b} and H_{uu_b}. Symbols and lines are as in Fig. 7.

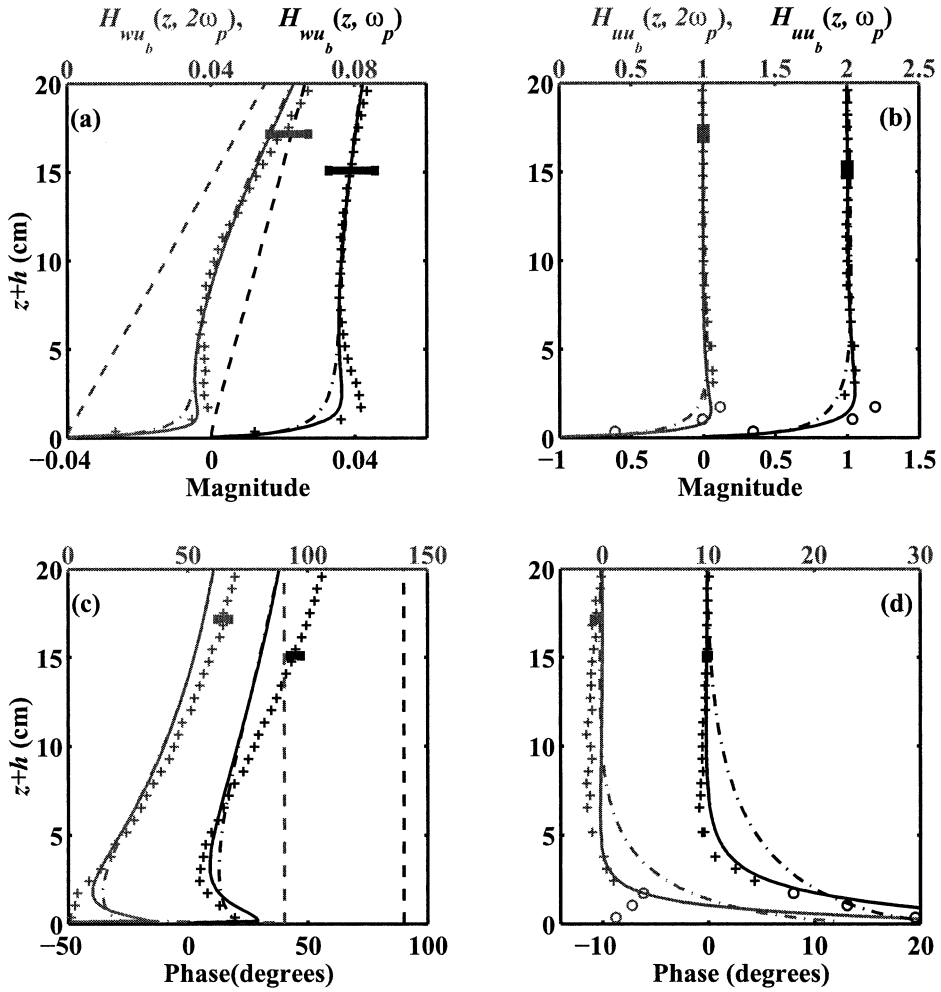

FIG. 9. Vertical profiles of the magnitude and phase of the transfer function (a),(c) H_{wu_b} and (b),(d) H_{uu_b} at the peak frequency (dark) and double the peak frequency (gray), for the flat bed interval. Scales for the transfer functions at $\omega_p(2\omega_p)$ are at the bottom (top) of each panel. Solid and dashed lines indicate the predictions from the viscoelastic model for $h_x = 2°$ and 0° respectively; dash–dot lines the conventional eddy viscosity model predictions for $h_x = 2°$. Measured data points (+); points (○) for u near the bed inferred from the vertical velocity using $u = -w/h_x$.

flat bed runs, however, the peak spectral densities for both S_{ww} and S_{uu}, are overpredicted by the sloping bed WBL models. The lower coherence during this interval is likely the source of the discrepancy (cf. Fig. 4 and section 3).

c. Shear stress

The Fourier transform of the horizontal component of the momentum equation (2.4), integrated with respect to z, yields the shear stress at frequency ω

$$\tau(\omega, z) = i\omega \int_z^{z_b} [u_b(\omega) - u(\omega, z)]\, dz, \quad (4.7)$$

where the shear stress at $z = z_b$, the reference height just outside of the WBL, is taken to be zero. Equation (4.7) may be rewritten as

$$\tau(\omega, z) = i\omega u_b(\omega) \int_z^{z_b} [1 - H_{uu_b}(\omega, z)]\, dz. \quad (4.8)$$

Thus, the observed transfer function between shear stress and the free stream velocity at the wave peak frequency, $H_{\tau u_b}(\omega_p, z)$, becomes

$$H^{\text{obs}}_{\tau u_b}(\omega_p, z) = \frac{\tau^{\text{obs}}(\omega_p, z)}{u_b^{\text{obs}}(\omega_p)} = i\omega_p \int_z^{z_b} [1 - H^{\text{obs}}_{uu_b}(\omega_p, z)]\, dz. \quad (4.9)$$

The observed profiles of magnitude and phase of the transfer function $H_{\tau u_b}(\omega_p, z)$ are compared with the predictions by the viscoelastic–diffusion and eddy viscosity models for the flat and rippled bed intervals in Figs. 14

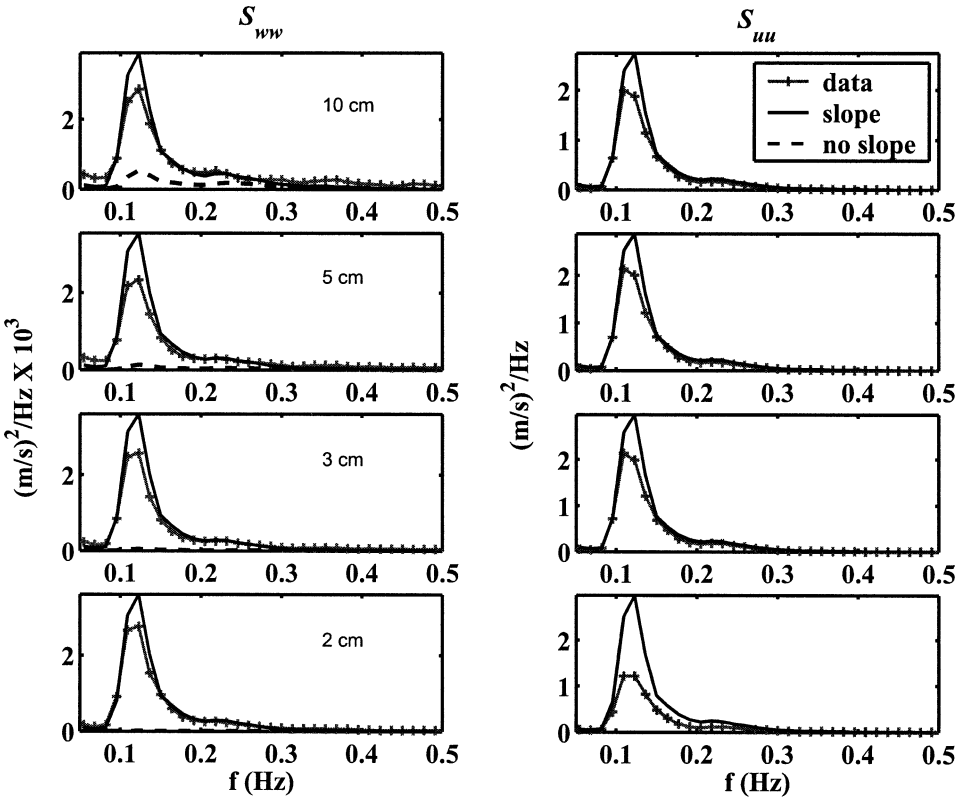

FIG. 10. Predicted and observed velocity spectra at 2, 3, 5, and 10 cm above bottom for rippled bed interval. Lines and symbols are as in Fig. 6.

and 15. The viscoelastic–diffusion model predictions give improved agreement with the observations compared to the eddy viscosity model for the flat bed case (Fig. 14). Note in particular the good agreement between the predicted magnitudes and the noninferred observed values (plus signs). The viscoelastic model underpredicts the observed phases, but less so than the standard eddy viscosity model. For the rippled bed interval, the agreement is not as good.

As pointed out by Sleath (1990), the momentum integral formula (4.9) for the shear stress involves subtraction of two large variables, u and u_b, so that it gives arise to significant error in case these two variables become identical to each other. It follows that the accuracy of the estimated shear stress decays rapidly near the top of the WBL where the horizontal velocity u approaches the free stream velocity u_b asymptotically. Such inaccuracy is visible in the shear-stress phase profile shown by Figs. 14 and 15, where the increasing phase difference between the shear stress and free stream velocity with height starts to taper off at about 4 cm above the bed. This behavior is in contrast with theory and laboratory observations. The accuracy of shear stress estimated by this method is also limited by the spatial resolution of the observed velocity profile.

5. Discussion

a. Bottom shear stress and bottom roughness

For beds consisting of mobile sediments, the bottom shear stress gives rise to the dynamic adjustment of the bed, including the development of bedforms and energy dissipating grain–grain interactions. The different bed state regimes are often characterized by different ranges of the grain roughness Shields parameter,

$$\theta = \frac{u_*^2}{(s - 1)gd},$$

where d is the sediment grain diameter, s is the sediment specific gravity, g is the gravitational acceleration, and u_* is computed using the friction factor from Eq. (A.1) and the nearbed wave orbital velocity amplitude. The grain roughness Shields parameters for the measurements discussed here, based on significant wave orbital velocity at 20 cm above the bed, were 0.3–0.4 for the rippled bed interval, and 0.6–0.8 for the flat bed interval (Table 1).

Friction velocity estimates can be obtained from the observed velocity profile by the momentum integral (MI) method based on the Eq. (4.9). Alternatively, the laboratory studies of oscillatory turbulent boundary layers by van Doorn (1982), Sleath (1987), and Jensen et

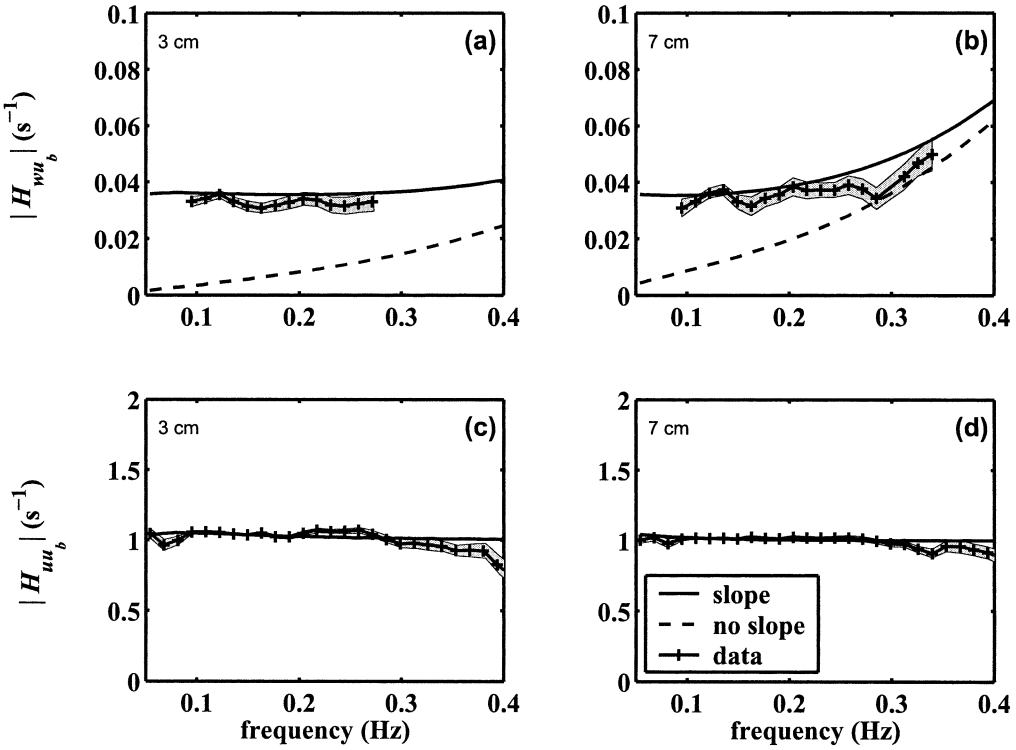

FIG. 11. Predicted and observed magnitudes of the transfer functions H_{wu_b} and H_{uu_b} vs frequency for the rippled bed interval. Symbols and lines are as in Fig. 7.

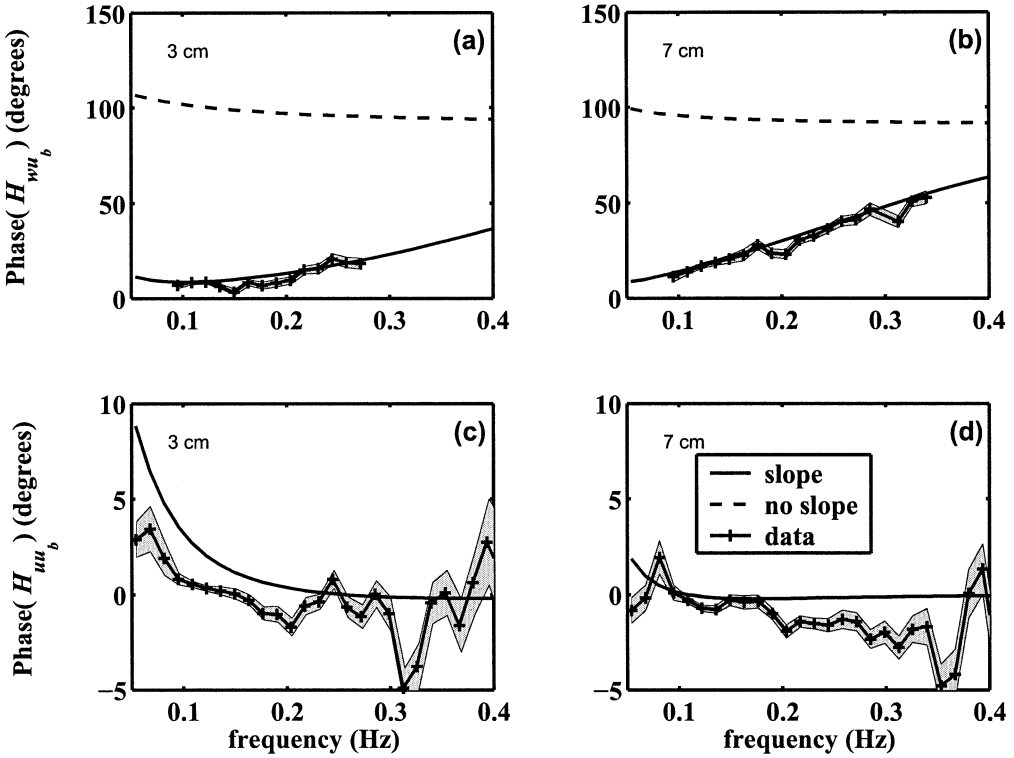

FIG. 12. Predicted and observed phases of the transfer functions H_{wu_b} and H_{uu_b} vs frequency for the rippled bed interval. Symbols and lines are as in Fig. 7.

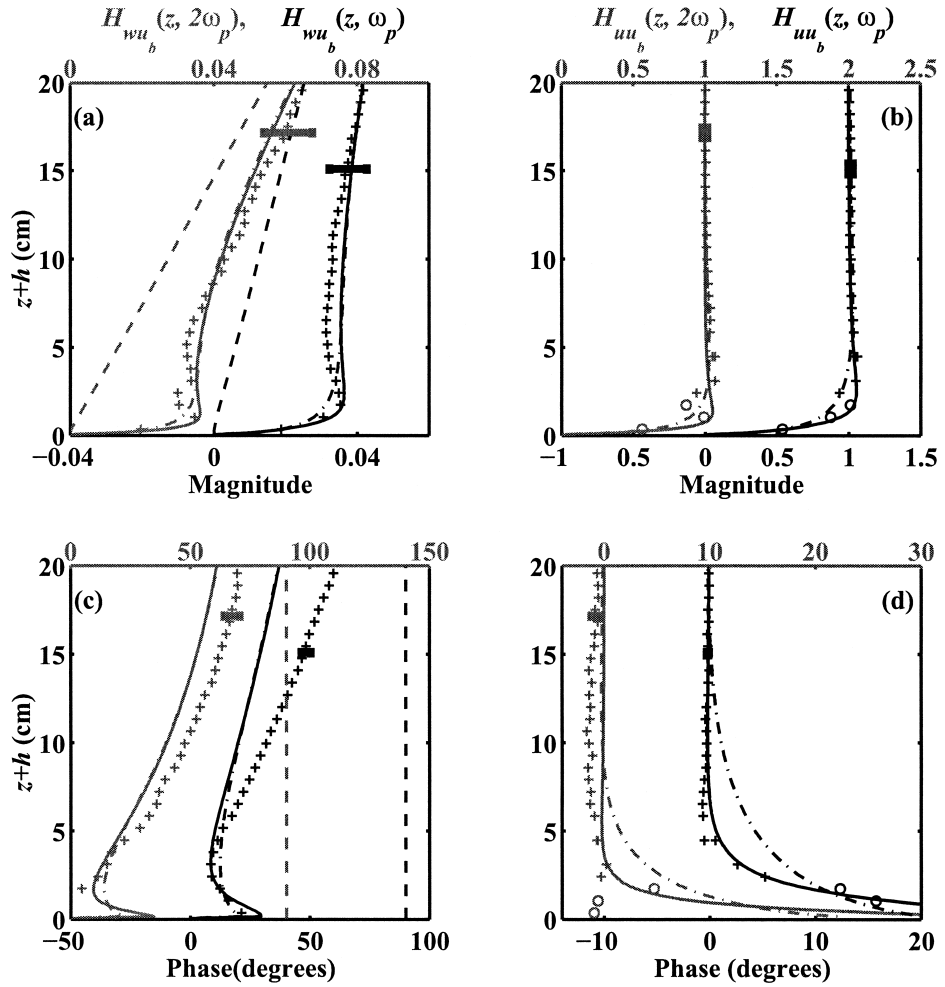

FIG. 13. Vertical profiles of the magnitude and phase of transfer functions (a),(c) H_{wu_b} and (b),(d) H_{uu_b} at the peak frequency (dark) and double the peak frequency (gray) for rippled bed interval. Scales for the transfer functions at $\omega_p(2\omega_p)$ are at the bottom (top) of each panel. Lines and symbols are as in Fig. 9.

al. (1989) suggest that a reasonable estimate of u_* is given by

$$u_* = \sqrt{2\langle w'^2 \rangle}, \tag{5.1}$$

where w' is the nearbed vertical turbulent velocity (cf. Smyth and Hay 2002) obtained by applying a 2-Hz cutoff frequency high-pass filter to the measured vertical velocity close to the bed: this is the vertical turbulence intensity (VTI) method. A third independent estimate of u_* can be obtained from the model best-fit values of the bottom roughness r_m (section 4a and Fig. 5).

Bottom roughnesses, friction factors and friction velocities determined using these three methods are listed in Tables 2 and 3. Values predicted using Nielsen's and Tolman's empirical formulas [appendix A, Eqs. (A.2)–(A.5)] are also shown for comparison. Numbers outside and inside parentheses are respectively based on taking the free stream velocity amplitude to be either that for the energy equivalent wave or the significant wave: that is, either $\sqrt{2}$ or 2 times the square root of the velocity variance.

The friction velocity estimates determined from the CDP data directly with the MI and VTI methods agree to within better than 20% for both intervals using the energy equivalent wave and to better than 10% using the significant equivalent wave. This close agreement provides additional support for the friction velocities and friction factors obtained by Smyth and Hay (2002) for a broader range of wave forcing and bed state conditions using the VTI method and a different MI method. The model-fit estimates of u_* are 20%–30% higher than the MI and VTI estimates.

The friction factor estimates for the flat bed and rippled bed intervals are approximately the same (for a given estimation method) despite the roughness and friction velocities being quite different. This is because the relative roughness r/a remains almost constant for both intervals.

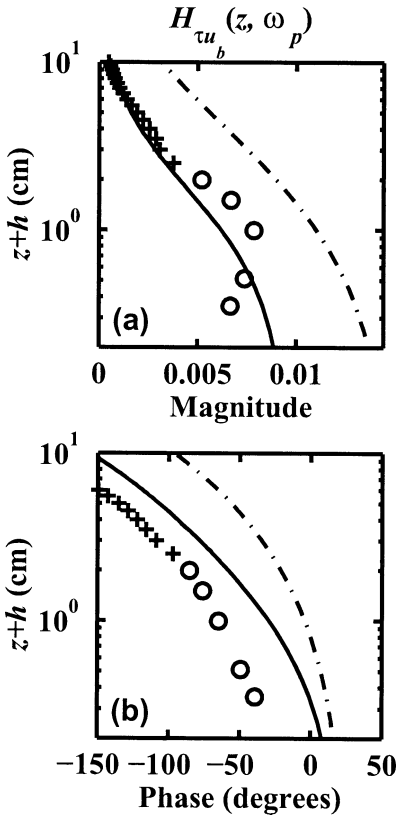

FIG. 14. Vertical profiles of the (a) magnitude and (b) phase of the transfer function $H_{\tau u_b}$ between the shear stress τ and the free stream velocity u_b at the wave peak frequency for the flat bed interval. Lines and symbols are as in Fig. 9.

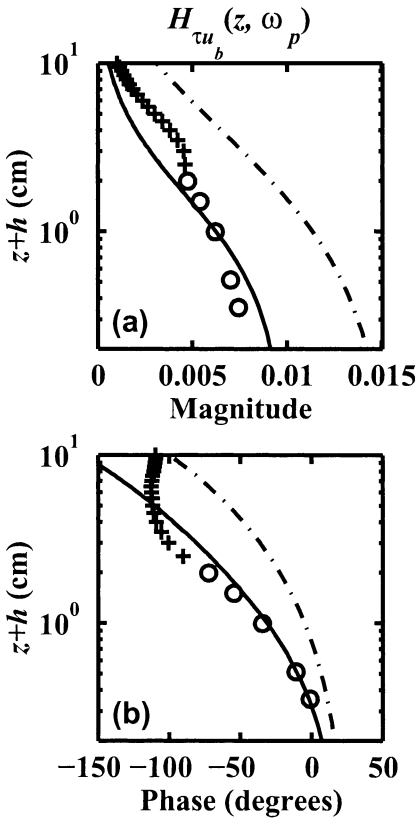

FIG. 15. As in Fig. 14 but for the rippled bed interval.

Last, the estimates of friction velocity from the CDP data are in approximate agreement with those given by Nielsen's (1992) and Tolman's (1994) semiempirical formulas. The agreement with Tolman's formula is better; Nielsen's formula overestimates the observations by up to 50% for both intervals.

b. WBL thickness

There is general agreement that the wave boundary layer thickness $\delta_w \sim Kl = K\kappa u_*/\omega$. The value of the constant K is not agreed upon, however, in part because it depends upon the definition of δ_w (see Jensen 1989). Grant and Madsen (1979) proposed a value of 2 for K. Smith (1977) proposed a value of 2.5, Christoffersen and Jonsson (1985) gave 0.367, and Jensen (1989) proposed 0.83. The smaller values of K correspond to inner measures of the thickness: the first height at which $u = u_b$ (Jonsson), or the height of maximum overshoot at a phase corresponding to wave crests (Jenssen). The larger values represent outer measures of the thickness. The values of δ_w listed in Tables 2 and 3 were computed using $K = 2$, and the peak frequencies in Table 1, and range from 3 up to 6 cm (nearly 8 cm if the results from

TABLE 2. Flat bed interval bottom roughness r, relative roughness r/a, wave friction factor f_w, friction velocity u_*, and WBL thickness δ_w estimated by optimizing the choice of physical roughness by minimizing the vertically integrated model–data discrepancy function (the viscoelastic and eddy viscosity methods), the momentum integration (MI) method, the vertical turbulence intensity (VTI) method, and the empirical formulas proposed by Nielsen (1992) and Tolman (1994). Numbers outside parentheses correspond to estimates made using the energy equivalent wave; those within parentheses correspond to the significant equivalent wave. The boldface numbers indicate the primary quantity (i.e., from which the others are derived) determined for a given method.

Method	r (cm)	$r/a \times 10^2$	$f_w \times 10^2$	u_* (cm s^{-1})	δ_w (cm)
Viscoelastic	**1.58 (0.63)**	3.0 (0.84)	2.0 (1.3)	5.1 (5.9)	5.4 (6.3)
Eddy viscosity	**0.40 (0.25)**	0.75 (0.33)	1.8 (1.4)	4.8 (6.0)	5.1 (6.4)
MI	0.50 (0.18)	0.93 (0.24)	1.4 (0.92)	**4.2 (4.9)**	4.5 (5.2)
VTI	0.18 (0.25)	0.33 (0.33)	1.0 (1.0)	**3.6 (5.1)**	3.8 (5.4)
Nielsen	**1.8 (2.5)**	3.4 (3.3)	2.1 (2.1)	5.2 (7.3)	5.5 (7.7)
Tolman	**0.38 (0.17)**	0.71 (0.22)	1.3 (0.9)	4.0 (4.8)	4.2 (5.1)

TABLE 3. As in Table 2 but for the rippled bed interval.

Method	r (cm)	$r/a \times 10^2$	$f_w \times 10^2$	u_* (cm s^{-1})	δ_w (cm)
Viscoelastic	**1.6 (0.79)**	3.5 (1.2)	2.1 (1.5)	4.3 (5.1)	4.6 (5.4)
Eddy viscosity	**0.50 (0.32)**	1.1 (0.49)	2.1 (1.6)	4.2 (5.2)	4.5 (5.5)
MI	0.56 (0.28)	1.2 (0.42)	1.5 (1.1)	**3.6 (4.3)**	3.8 (4.6)
VTI	0.13 (0.23)	0.3 (0.35)	0.97 (1.0)	**2.9 (4.2)**	3.1 (4.5)
Nielsen	**1.5 (2.1)**	3.3 (3.26)	2.1 (2.2)	4.4 (6.2)	4.7 (6.6)
Tolman	**0.79 (0.28)**	1.7 (0.42)	1.7 (1.1)	3.9 (4.3)	4.1 (4.6)

Nielson's formula are included). These boundary layer thicknesses are comparable to the values 2.7 and 3.4 cm determined by Trowbridge and Agrawal (1995), also using $K = 2$, and furthermore are quite realistic in comparison with the heights at which the observed vertical velocity magnitudes exhibit overshoot (Figs. 9a and 13a). (Recall that the vertical velocity in the WBL over a sloping bed is highly dependent upon u.) In addition, the observed vertical velocity profiles suggest that the WBL thickness at double the peak frequency is about one-half that at the peak frequency, as expected.

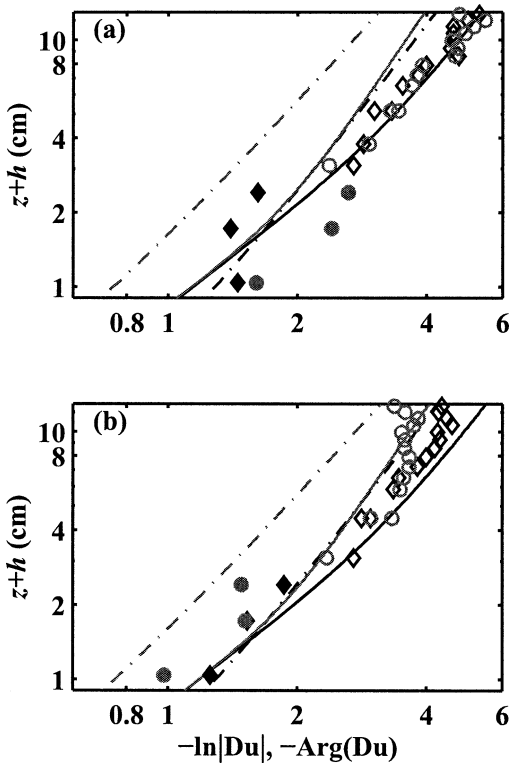

FIG. 16. Predicted and measured dimensionless complex velocity defect at the wave peak frequency, $Du(\omega_p, z) = 1 - H_{uu_b}(\omega_p, z)$ for (a) flat bed interval and (b) rippled bed interval. Solid lines represent viscoelastic–diffusion model predictions; dashed lines are the standard eddy viscosity model. The data are open symbols; inferred data from vertical velocity measurements at the same point using relationship $u = -w/h_x$ are filled symbols. Black lines and symbols indicate $-\ln|Du|$; gray lines and symbols show $-\arg(Du)$.

c. Velocity defect

For a monochromatic wave turbulent boundary layer, the nondimensional velocity defect is defined as $Du(z) = [u_b(t) - u(z, t)]/u_b(t)$. Nielsen (1984) found that the relationship $\log|Du| \equiv \arg(Du)$, derived from the laminar boundary layer solutions, holds well for laboratory measurements of the turbulent WBL over a rough bed by Jonsson and Carlson (1976) and van Doorn (1982). Conventional eddy viscosity and mixing length models, however, predict a fairly large difference between these two quantities (Nielsen 1992; Zou 2002).

For spectral waves, a frequency-dependent nondimensional velocity defect can be constructed from the transfer function between the horizontal velocity $u(z, t)$ and the free stream velocity $u_b(t)$: thus, at the wave peak frequency ω_p, $Du(\omega_p, z) = 1 - H_{uu_b}(\omega_p, z)$. The observed profiles of $-\ln|Du|$ and $-\arg(Du)$ at the wave peak frequency are presented in Figs. 16a and 16b and, as observed by Nielsen (1984, 1992) for laboratory measurements, are very similar. This behavior is reproduced by the viscoelastic–diffusion model, but not by the standard eddy viscosity model. This finding is similar to that by Zou (2002) from comparisons of these models with laboratory measurements.

d. Goodness-of-fit of velocity profiles

Root-mean-square differences between the model-predicted and observed magnitude and phase profiles at the wave peak frequency in Figs. 9 and 13 are listed in Table 4 for the flat and rippled bed intervals, respectively. The rms differences were computed as follows:

$$\Delta_{|u|} = \frac{\int_0^{z_u} [|H^{\text{pred}}_{uu_b}(\omega, z)| - |H^{\text{obs}}_{uu_b}(\omega, z)|]^2 \, dz}{\int_0^{z_u} |H^{\text{obs}}_{uu_b}(\omega, z)|^2 \, dz}, \tag{5.2}$$

$$\Delta_{|w|} = \frac{\int_0^{z_u} [|H^{\text{pred}}_{wu_b}(\omega, z)| - |H^{\text{obs}}_{wu_b}(\omega, z)|]^2 \, dz}{\int_0^{z_u} |H^{\text{obs}}_{wu_b}(\omega, z)|^2 \, dz}, \tag{5.3}$$

TABLE 4. Root-mean-square magnitude and phase differences between model-predicted and observed velocity transfer functions at the wave peak frequency in the WBL. The rms differences were computed over the 10-cm interval off the bed (excluding u at the three data points closest to the bed).

	Flat bed interval				Rippled bed interval			
Method	$\Delta_{\lvert u\rvert}$ (%)	$\Delta_{\lvert w\rvert}$ (%)	$\Delta\vartheta_u$ (°)	$\Delta\vartheta_w$ (°)	$\Delta_{\lvert u\rvert}$ (%)	$\Delta_{\lvert w\rvert}$ (%)	$\Delta\vartheta_u$ (°)	$\Delta\vartheta_w$ (°)
Viscoelastic	0.24	0.75	1.1	4.9	0.11	0.94	1.0	7.1
Eddy viscosity	0.80	1.80	3.7	5.1	0.18	1.05	3.3	6.3

$$\Delta\vartheta_u = \left\langle z_u^{-1} \int_0^{z_u} \{\arg[H_{uu_b}^{\text{pred}}(\omega_p, z)] - \arg[H_{uu_b}^{\text{obs}}(\omega_p, z)]\}^2 \, dz \right\rangle^{1/2}, \quad (5.4)$$

and

$$\Delta\vartheta_w = \left\langle z_u^{-1} \int_0^{z_u} \{\arg[H_{wu_b}^{\text{pred}}(\omega_p, z)] - \arg[H_{wu_b}^{\text{obs}}(\omega_p, z)]\}^2 \, dz \right\rangle^{1/2}. \quad (5.5)$$

The upper limit integration $z_u = 10$ cm. The rms phase differences were not normalized to avoid biasing the result by the near-zero phases at the top of the boundary layer; u at the three data points closest to the bed was excluded in the calculation.

The results in Table 4 indicate overall goodness of fits better than 1% in the relative magnitude of H_{uu_b}, at both ω_p. The $|H_{wu_b}|$ fits are not as good (2% or better), but they are still acceptable. The rms differences in the phase of H_{uu_b} are 3° or better; and they are 10° or better for H_{wu_b}. Comparing the corresponding values for the two models, it can be seen that the viscoelastic–diffusion model predictions are either very similar to or an improvement on the standard eddy viscosity model for this dataset: the greatest improvements are in the phase of H_{uu_b}, as expected from Figs. 9d and 13d, and in the magnitude of H_{uu_b}.

6. Summary and conclusions

Theoretical predictions of near-bed velocity and shear stress profiles within the WBL above a sloping bottom have been shown to be in quantitative agreement with field observations acquired with a high-resolution pulse-coherent Doppler profiler on a planar beach outside the surf zone. Two analytic solutions for the WBL velocities are used in the comparisons, one using a complex eddy viscosity based on the Bradshaw–Ferris–Atwell and Townsend (BFA-T) form of the turbulent kinetic energy equation (the viscoelastic–diffusion model; Zou 2002), the other a conventional real-valued eddy viscosity (which we call the standard eddy viscosity model). Both models incorporate the sloping bottom effect, and both assume linear relationship between local sea surface elevation and velocity at depth. The velocity solutions for the WBL are formally equivalent to the corresponding horizontal bed case: the sloping bed effect on the WBL enters the theory through free stream velocity. The free stream velocity is matched with the wave bottom orbital velocity outside the WBL, obtained from the observed local surface elevation using the Chu and Mei inviscid theory for (linear) surface gravity waves over a sloping bed. The surface elevation measurements were collected with an upward-looking acoustic sounder. Model–data comparisons are carried out for both flat bed and (linear transition) rippled bed conditions, for significant wave height to water depth ratios of 0.30 to 0.24, and for both distinctly bimodal and nearly unimodal incident wave spectra.

Generally good agreement is found between the observed and predicted profiles of vertical and horizontal velocity in both magnitude and phase. Better agreement is obtained with the viscoelastic model compared to the standard eddy viscosity model, particularly within the bottom 5 cm of the profiles (i.e., within the WBL). The largest difference between these two sets of model predictions is in the vertical profile of the horizontal velocity phase: the u phase profile is well predicted by the viscoelastic model, but not by the standard model. We also find that the sloping bottom has significant effects on the vertical velocity but not on the horizontal velocity and shear stress.

Linear WBL theory adequately describes the complex-valued transfer function between the velocities through the WBL and the wave bottom orbital velocity over the sea and swell wave frequency band (0.05–0.3 Hz). This result arises despite the expectation of significant nonlinear effects at harmonic frequencies for this dataset. It indicates that the local vertical transformations of free and forced waves are indistinguishable within the WBL.

Turbulent shear stress profiles, obtained from the observed velocity profiles, are predicted reasonably well by the viscoelastic model for the flat bed interval. The predicted stress magnitude profile is in good agreement with the observations, while the observed phase profile is overestimated by 30°–50°, depending on height. The stress profile predictions from the standard model for the flat and rippled bed intervals differ significantly

from the observations in both magnitude and phase at all heights.

The model-based best-fit estimate of bottom roughness compares favorably (i.e., to within 20%–30%) with the estimates based on the nearbed vertical turbulence intensity, and on the observed horizontal velocity by the momentum integral method. These values are also consistent (to within a factor of 20%) with estimates from Tolman's (1994) semiempirical formulation.

Velocity overshooting within the WBL is clearly indicated in the observed vertical velocity profiles, but not in the observed horizontal velocity profiles. The absence of clearly defined overshoot in the observed u profiles is due to the fact that the predicted overshoot in u is weak and occurs between 2 and 3 cm above the bed where the CDP measurements of horizontal velocity are contaminated by the reflected acoustic pulse through the transducer beam pattern side lobes. There is, however, pronounced overshoot in the observed w profiles at a height between 1 and 5 cm, which is well reproduced by the viscoelastic model with bottom slope, but less well by the standard model. The w measurements are not affected by the sidelobe problem.

Thus, it is concluded that including the turbulent relaxation and vertical diffusion terms in the BFA-T turbulent energy equation leads to a complex eddy viscosity that gives improved predictions of velocity profiles within the WBL for spectral waves in field conditions as compared with the standard time-invariant eddy viscosity model. A similar conclusion was drawn previously, for monochromatic waves over a horizontal bottom, from comparisons of the present theory with laboratory measurements (cf. Zou 2002). The viscoelastic model has several advantages. First, the complex eddy viscosity introduces a phase shift between shear stress and velocity gradient that varies with the height above the bed, which is more realistic than the conventional real-valued eddy viscosity. Second, as compared with time-varying eddy viscosity models, it is more readily applied to the irregular wave fields typical of field conditions: the comparisons can be made on the basis of run-length statistical properties, without having to carry out a wave by wave, phase-based analysis, for example. Third, the analytical nature of the model allows it to be readily adapted to and tested under field conditions, as has been done here for a sloping bed.

Acknowledgments. We thank A. J. Bowen and R. T. Guza for helpful discussions of bottom slope effects, L. Zedel and C. Smyth for discussion and the initial processing of the CDP data, and P. Nielsen for drawing our attention to the dimensionless velocity defect. A preliminary draft of this paper was completed while Q.-P. Zou was visiting the Applied Ocean Physics and Engineering Department at the Woods Hole Oceanographic Institution. She wishes to thank people there, particularly J. H. Trowbridge and J. F. Lynch, for their hospitality and stimulating discussion. This research was supported by the Coastal Sciences Program of the U.S. Office of Naval Research and the Natural Science and Engineering Research Council of Canada.

APPENDIX A

Roughness Length

The equivalent roughness r and friction factor f_w are related by the following empirical formula of Nielsen (1992):

$$f_w = \exp\left[5.213\left(\frac{r}{A}\right)^{0.194} - 5.977\right], \qquad \text{(A.1)}$$

where A is the wave orbital amplitude just above the boundary layer. Nielsen (1992) derived the following empirical estimate of equivalent roughness:

$$\begin{aligned} r &= 70\sqrt{\theta}d \\ &= 170\sqrt{\theta_{2.5} - 0.05}d \quad \text{for } \theta > 0.5, \end{aligned} \qquad \text{(A.2)}$$

where d is the sediment grain diameter, $\theta = u_*^2/[(s - 1)gd]$ is the Shields parameter, u_*^2 is the peak bed shear stress,

$$\theta_{2.5} = \frac{1}{2}\frac{f_{2.5}(A\omega)^2}{(s - 1)gd}$$

is the grain roughness Shields parameter, $f_{2.5}$ is given by (A.1) with $r = 2.5d_{50}$, and d_{50} is the median grain size. Accordingly, Nielsen (1992) estimated that the relative equivalent roughness, r/A, of a flat bed with loose sand under waves ranges from 0.085 to 1.15.

The roughness for a rippled bed under waves is (cf. Nielsen 1992)

$$r = 8\eta^2/\lambda + 170\sqrt{\theta_{2.5} - 0.05}d, \qquad \text{(A.3)}$$

where η is the ripple height and λ is the ripple wave length. The second term accounts for the movable bed roughness as shown in (A.2) for a flat bed.

Following Tolman (1994), one may also use the equivalent bottom roughness given by Wilson (1989) for sheet flow; that is,

$$r_s = 0.0655A\left[\frac{(A\omega)^2}{(s - 1)gA}\right]^{1.4}, \qquad \text{(A.4)}$$

and the mobile bed roughness for spectral waves proposed by Madsen et al. (1990) for a rippled bed:

$$r_r = 1.5A\left(\frac{\theta}{\theta_c}\right)^{-2.5} \quad \text{for } \theta \geq 1.2\theta_c, \qquad \text{(A.5)}$$

where θ_c is the critical Shields parameter for sediment motion and will be taken as 0.05 (Nielsen 1992).

APPENDIX B

Representative Wave

When the wave energy is distributed over a range of frequencies, Mathisen and Madsen's (1999) laboratory

measurements demonstrated that a representative bottom roughness can be used for all wave components (cf. Madsen 1994). Given the bottom roughness, the bottom friction is assumed to be equivalent to that experienced by a representative monochromatic wave, and the bottom friction can be used to evaluate the WBL solutions for each wave component to construct the WBL solutions under an arbitrary wave forcing (cf. Trowbridge and Agrawal 1995; Beach and Sternberg 1992; Madsen and Wikramanayake 1991). Such an approach is only valid if the vertical structure of each wave component resembles that of a free wave. This underlying hypothesis has been verified for the irrotational flow above the WBL in the field by Guza and Thornton (1980) and Herbers et al. (1992) and by the theoretical investigation by Zou et al. (2003), but not yet in the field for flow within the WBL.

A commonly used equivalent monochromatic wave is one with the same velocity variance as the spectral wave and a frequency equal to the energy-weighted average frequency, namely,

$$u_r = \left[\int 2S_{uu}(\omega)\, d\omega\right]^{1/2} \equiv \left(\int \frac{2\omega^2}{\sinh^2 kh} S_{\eta\eta}\, d\omega\right)^{1/2}, \quad \text{(B.1)}$$

$$\omega_r = \frac{\int S_{uu}(\omega)\omega\, d\omega}{\int S_{uu}(\omega)\, d\omega}, \quad \text{(B.2)}$$

$$A_r = \frac{u_r}{\omega_r}, \quad \text{(B.3)}$$

where $S_{\eta\eta}$ and S_{uu} are the power spectral densities of the surface elevation and the free stream velocity (Madsen 1994); u_r, ω_r, and A_r are the representative wave bottom velocity, wave frequency, and semiexcursion amplitude of wave orbital motion.

Given a bottom roughness length r and semiexcursion amplitude of A_r, the equivalent wave friction factor f_{wr} for viscoelastic–diffusion and conventional eddy viscosity models may be derived as a function of relative roughness r/A_r (cf. Zou 2002), and the equivalent bottom friction velocity becomes

$$u_* = u_{*r} = \left(\frac{1}{2} f_{wr} u_r^2\right)^{1/2}. \quad \text{(B.4)}$$

REFERENCES

Abramowitz, M., and I. A. Stegun, 1970: *Handbook of Mathematical Functions.* U.S. Natl. Bur. Stand., 1046 pp.

Ardhuin, F., T. H. C. Herbers, and W. C. O'Reilly, 2001: A hybrid Eulerian–Lagrangian model for spectral wave evolution with applications to bottom friction on the continental shelf. *J. Phys. Oceanogr.,* **31,** 1498–1516.

Beach, R. A., and R. W. Sternberg, 1992: Suspended sediment transport in the surf zone: Response to incident wave and longshore current interaction. *Mar. Geol.,* **108,** 275–294.

Bendat, J. S., and A. G. Piersol, 1986: *Random Data: Analysis and Measurement Procedures.* Wiley-Interscience, 566 pp.

Bijker, E. W., J. P. T. Kalwijk, and T. Pieters, 1974: Mass transport in gravity waves on a sloping bottom. *Proc. ASCE 14th Int. Coastal Engineering Conf.,* Copenhagen, Denmark, ASCE, 447–465.

Bradshaw, P., D. H. Ferris, and N. P. Atwell, 1967: Calculation of boundary layer development using the turbulent kinetic energy equation. *J. Fluid Mech.,* **30,** 241–258.

Brevik, I., 1981: Oscillatory rough turbulent boundary layers. *J. Waterway, Port, Coastal Ocean Div.,* **107** (WW3), 175–188.

Christoffersen, J. B., and I. G. Jonsson, 1985: Bed friction and dissipation in a combined current and wave motion. *Ocean Eng.,* **12,** 387–423.

Chu, V. H., and C. C. Mei, 1970: On slowly varying Stokes waves. *J. Fluid Mech.,* **41,** 873–887.

Crawford, A. M., and A. E. Hay, 1999: A simple system for laser-illuminated video imaging of sediment suspension and bed topography. *IEEE J. Oceanic Eng.,* **23,** 12–19.

——, and ——, 2001: Linear transitional ripple migration and wave orbital velocity skewness: Observations. *J. Geophys. Res.,* **106** (C7), 14 113–14 128.

Davies, A. G., 1986: A model of oscillatory rough turbulent boundary layer flow. *Estuarine Coastal Shelf Sci.,* **23,** 353–374.

Dingler, J. R., and D. L. Inman, 1976: Wave-formed ripples in nearshore sands. *Proc. 15th Int. Coast. Eng. Conf.,* Vol. 2, Honolulu, HI, ASCE, 2109–2126.

Foster, D. L., 1996: Dynamics of the nearshore wave bottom boundary layer. Ph.D. thesis, Oregon State University, 114 pp.

Fredsoe, J., and R. Deigaard, 1992: *Mechanics of Coastal Sediment Transport.* World Scientific, 369 pp.

Grant, W. D., 1977: Bottom friction factor under waves in the presence of a weak current: Its relationship to coastal sediment transport. Sc.D. thesis, Massachussets Institute of Technology, Cambridge, MA, 275 pp.

——, and O. S. Madsen, 1979: Combined wave and current interaction with a rough bottom. *J. Geophys. Res.,* **84,** 1797–1808.

——, and ——, 1986: The continental shelf bottom boundary layer. *Annu. Rev. Fluid Mech.,* **18,** 265–305.

Guza, R. T., and E. B. Thornton, 1980: Local and shoaled comparisons of sea surface elevations, pressures, and velocities. *J. Geophys. Res.,* **85,** 1524–1530.

Hay, A. E., and D. Wilson, 1994: Rotary sidescan images of nearshore bedform evolution during a storm. *Mar. Geol.,* **119,** 57–65.

Herbers, T. H. C., R. L. Lowe, and R. T. Guza, 1992: Field observations of orbital velocities and pressure in weakly nonlinear surface gravity waves. *J. Fluid Mech.,* **245,** 413–435.

Jensen, B. L., 1989: Experimental investigation of turbulent oscillatory boundary layers. IHHE Series Paper 45, Technical University of Denmark, 157 pp.

——, B. L. Sumer, and J. Fredsoe, 1989: Turbulent oscillatory boundary layers at high Reynolds numbers. *J. Fluid Mech.,* **116,** 265–298.

Johns, B., 1969: On the mass transport induced by oscillatory flow in a turbulent boundary layer. *J. Fluid. Mech.,* **43,** 177–185.

Jonsson, I. G., 1966: Wave boundary layers and friction factors. *Proc. 10th Int. Conf. on Coastal Engineering,* Tokyo, Japan, ASCE, 127–148.

——, and N. A. Carlsen, 1976: Experimental and theoretical investigations in an oscillatory turbulence boundary layer. *J. Hydraul. Res.,* **14,** 45–60.

Kajiura, K., 1968: A model of the bottom boundary layer in water waves. *Bulletin Earthquake Res. Inst.,* **46,** 75–123.

Lavelle, J. W., and H. O. Mofjeld, 1983: Effects of time-varying viscosity on oscillatory turbulent channel flow. *J. Geophys. Res.,* **88** (C12), 7607–7616.

Madsen, O. S., 1994: Spectral wave-current bottom boundary layer

flows. *Proc. 24th Int. Conf. on Coastal Engineering*, Vol. 1, Kobe, Japan, ASCE, 384–398.
——, and P. N. Wikramanayake, 1991: Simple model for turbulent wave-current bottom boundary layer flow. Contract Rep. DRP-91-1, U.S. Army Corps of Engineers, Coastal Engineering Research Center, Vicksburg, MS, 150 pp.
——, P. P. Mathiesen, and M. M. Rosengaus, 1990: Movable bed friction factors for spectral waves. *Proc. 22d Int. Conf. on Coastal Engineering*, Delft, Netherlands, ASCE, 420–429.
Mathisen, P. P., and O. S. Madsen, 1999: Waves and currents over a fixed rippled bed. 3. Bottom and apparent roughness for spectral waves and currents. *J. Geophys. Res.*, **104** (C8), 18 447–18 461.
Myrhaug, D., 1982: On a theoretical model of rough turbulent wave boundary layers. *Ocean Eng.*, **9,** 547–565.
Ngusaru, A. S., and A. E. Hay, 2003: Cross-shore migration of lunate megaripples during Duck94. *J. Geophys. Res.*, in press.
Nielsen, P., 1984: On the structure of oscillatory boundary layers. *Coastal Eng.*, **9,** 261–276.
——, 1992: *Coastal Bottom Boundary Layers and Sediment Transport.* World Scientific, 324 pp.
Sleath, J. F. A., 1987: Turbulent oscillatory flow over rough beds. *J. Fluid Mech.*, **182,** 369–409.
——, 1990: Seabed boundary layers. *The Sea,* B. LeMehaute and D. M. Hanes, Eds., Ocean Engineering Science, Vol. 9, John Wiley and Sons, 693–727.
Smith, J. D., 1977: Modelling of sediment transport on continental shelves. *The Sea*, E. D. Goldberg et al., Eds., Marine Modeling, Vol. 6, John Wiley and Sons, 539–577.
Smyth, C., and A. E. Hay, 2002: Wave friction factors in nearshore sands. *J. Phys. Oceanogr.*, **32,** 3490–3498.
——, ——, and L. Zedel, 2002: Coherent Doppler profiler measurements of near-bed suspended sediment fluxes and the influence of bed forms. *J. Geophys. Res.*, **107,** 3105, doi:10.1029/2000JC000760.
Tolman, H. L., 1994: Wind waves and moveable-bed bottom friction. *J. Phys. Oceanogr.*, **24,** 994–1009.
Townsend, A. A., 1972: Flow in a deep turbulent boundary layer over a surface distorted by water waves. *J. Fluid Mech.*, **55,** 719–735.
Trowbridge, J. H., and O. S. Modsen, 1984: Turbulent wave boundary layers. I. Model formulation and first-order solution. *J. Geophys. Res.*, **89** (C5), 7987–7997.
——, and Y. C. Agrawal, 1995: Glimpses of a wave boundary layer. *J. Geophys. Res.*, **100** (C10), 20 729–20 743.
van Doorn, T., 1982: Experimenteel onderzoek naar het snelheidsveld in de turbulente bodemgrenslaag in een oscillerende stroming in een golftunnel. Delft Hydraulics Laboratory Rep. M1562-1b.
Wilson, K. C., 1989: Friction of wave-induced sheet flow. *Coastal Eng.*, **12,** 371–379.
Young, I. R., and R. M. Gorman, 1995: Measurements of the evolution of ocean wave spectra due to bottom friction. *J. Geophys. Res.*, **100** (C6), 10 987–11 004.
Zedel, L., and A. E. Hay, 1999: A coherent Doppler profiler for high resolution particle velocimetry in the ocean: Laboratory measurements of turbulence and particle flux. *J. Atmos. Oceanic Technol.*, **16,** 1102–1117.
——, and ——, 2002: A three component bistatic coherent Doppler velocity profiler: Error sensitivity and system accuracy. *IEEE J. Oceanic Eng.*, **27,** 717–725.
Zou, Q.-P., 1995: A viscoelastic model for turbulent flow over an undulating topography and progressive waves. Ph.D. thesis, Scripps Institution of Oceanography, 91 pp.
——, 1998: A viscoelastic model for turbulent flow over an undulating topography. *J. Fluid Mech.*, **355,** 81–112.
——, 2002: An analytical model of wave bottom boundary layers incorporating turbulent relaxation and diffusion effects. *J. Phys. Oceanogr.*, **32,** 2441–2456.
——, and A. E. Hay, 2001: Velocity profiles above and within the wave bottom boundary layer over a sloping bottom. *Proc. 27th Int. Coastal Engineering Conf.*, Sydney, Australia, ASCE, 94–107.
——, ——, and A. J. Bowen, 2003: The vertical structure of surface gravity waves propagating over a sloping sea bed: Theory and field measurements. *J. Geophys. Res.*, in press.